Variable X-Ray Emission of Comet 46P/Wirtanen

Emanuele Bonamente, Damian J Christian, Zexi Xing, Kumar Venkataramani, Dimitra Koutroumpa, Dennis Bodewits

The Planetary Science Journal, 2:224 (23pp), 2021 December https://doi.org/10.3847/PSJ/ac2aac

Variable X-Ray Emission of Comet 46P/Wirtanen

Emanuele Bonamente[1], Damian J. Christian[2], Zexi Xing (邢泽曦)[1,3], Kumar Venkataramani[1], Dimitra Koutroumpa[4], and Dennis Bodewits[1]
[1] Physics Department, Leach Science Center, Auburn University, Auburn, AL 36832, USA; dennis@auburn.edu
[2] Department of Physics and Astronomy, California State University, Northridge, CA, 91330, USA
[3] Department of Physics and Laboratory for Space Research, The University of Hong Kong, Hong Kong SAR, People's Republic of China
[4] LATMOS/IPSL, CNRS, UVSQ Paris Saclay, Sorbonne Université, Guyancourt, France
Received 2020 October 4; revised 2021 September 23; accepted 2021 September 25; published 2021 November 9

Abstract

In this paper, we present an analysis of X-ray and optical/ultraviolet (UV) data from the favorable ($\Delta \sim 0.077$ au) 2018 apparition of comet 46P/Wirtanen. The comet was observed during three different epochs (before, during, and after perihelion) over a 1.5 month period using the X-Ray Telescope (XRT) and Ultraviolet and Optical Telescope (UVOT) instruments on board the Neil Gehrels Swift Observatory and the Advanced CCD Imaging Spectrometer (ACIS) on board the Chandra X-ray Observatory. We clearly detected the comet's charge exchange-induced emission during the first two epochs ($F_x = (11.2 \pm 0.8)$ and $(6.9 \pm 0.5) \times 10^{-13}$ erg cm^{-2} s^{-1}, respectively), while only an upper limit on the flux could be placed for the third epoch ($F_x < 1.38 \times 10^{-13}$ erg cm^{-2} s^{-1}). As such, 46P/Wirtanen is one of the least luminous comets to be detected in X-rays. X-ray emission from the charge exchange between solar wind ions and the neutrals in the coma were analyzed against the water-production rate (Swift/UVOT) and space weather measurements. Further analyses of the emission features show that the solar wind properties inferred from the observed X-ray spectrum are in good agreement with those measured by the Advanced Composition Explorer (ACE) and Solar and Heliospheric Observatory (SOHO) spacecraft, proving the approach is reliable for solar wind diagnostics. It is also found that, despite the variability of the comet's properties (e.g., the water-production rate used as a neutrals density proxy), cometary X-ray emission is primarily modulated by the solar wind.

Unified Astronomy Thesaurus concepts: Comets (280); Charge exchange recombination (2062); Solar wind (1534)

Supporting material: machine-readable table

1. Introduction

Our interest in comets resides in the fact that they bear traces of the environment out of which our solar system formed (Busemann et al. 2009) and potentially contributed to the composition of the Earth's atmosphere (Pollack & Yung 1980; Rubin et al. 2019). The interaction of comets with the solar wind is analogous to that of planets with no significant magnetic fields (i.e., Mars and Venus; Neugebauer et al. 2000; Schwadron & Cravens 2000; Cravens 2002). As extended objects that move around the solar system, comets provide us with a unique laboratory, allowing us to remotely study the solar wind properties at otherwise inaccessible locations and the plasma interactions in variable solar wind conditions.

Charge exchange-induced emission from comets happens when highly charged solar wind ions interact with neutral molecules in the coma, producing highly excited ions that emit ultraviolet (UV) and X-ray photons (Cravens 1997). As a comet approaches the Sun, the nucleus heats up, and part of the frozen volatiles (mainly H_2O) sublimate, creating an expanding exosphere (i.e., the coma). When exposed to the solar wind, charge exchange between solar wind ions and cometary neutrals can produce up to 1 GW in soft X-ray luminosity (Lisse et al. 2013). This emission can be used as a diagnostic of the local solar wind parameters because the observed X-ray spectrum reflects the composition, ionization state, and velocity of the solar wind particles (Bodewits et al. 2007). Open questions remain on how the charge-exchange emission depends on the neutral gas content, and particularly how H_2O and CO_2 production rates contribute to the observed X-ray variability (Krasnopolsky et al. 2000) and how they affect X-ray spectra (Mullen et al. 2017).

46P/Wirtanen (hereafter 46P) is a Jupiter-family, short-period comet (5.4 yr) that was the original target of the Rosetta mission (Schwehm & Schulz 1999). As such, it has been intensively studied in the past, resulting in a detailed characterization of the size of its nucleus (Lamy et al. 1998), its dust environment (Fulle 2000), its gas-production rates (Farnham & Schleicher 1998), and its rotational state (Meech et al. 1997). Interest in comet 46P has not diminished, even after the Rosetta mission was redirected to comet 67P/Churyumov-Gerasimenko (Glassmeier et al. 2007). A particularly favorable apparition in late 2018 to early 2019 (geocentric distance ~0.077 au) offered the opportunity to plan numerous Earth- and space-based observation campaigns (e.g., Warner et al. 2016; DiSanti et al. 2017; Bodewits et al. 2019; Noonan et al. 2021). Comet 46P is one of the few comets classified as hyperactive because of its high gas-production rate compared with the small size of its nucleus (Lamy et al. 1998). Recent observations support the presence of extended sources (i.e., icy grains) that contribute significantly to the water-production rate (Combi et al. 2019a). Unlike comet 103P/Hartley, however, for which the hyperactivity is driven by CO_2 (A'Hearn et al. 2011), UV observations of 46P show no evidence of abundant CO_2 (Stern et al. 1998; Noonan et al. 2021; K. Venkataramani, 2022, in preparation). Finally, comet 46P is also characterized by a low dust-to-gas ratio (de Almeida et al. 2007), limiting the contribution of light scattering from dust. Here, we present analysis of the

observations of comet 46P in X-ray and optical/UV bands with the main goal of investigating what drives the time variability of X-ray emission. For this, we correlate the X-ray emission with comet properties (i.e., gas-production rate) and solar wind characteristics (i.e., density, velocity, and abundance of solar wind charged particles). Section 2 describes the Swift and Chandra observations, details of the data-reduction process, and the sources of solar wind data. The results of the observations during each of the three observing epochs are presented in Section 3. Section 4.2 provides a quantitative comparison of the X-ray emission in the three epochs based on measurements of the comet's production rate and solar wind properties acquired at L1. In addition, we discuss the relation between X-ray and optical emission of comets in Section 4.2. Conclusions are given in Section 5. The complete logs and observing geometry of the Swift and Chandra observations used in this study are given in the Appendix as observations of moving objects are often hard to locate in coordinate-based astrophysical data archives.

2. Observations and Data Reduction

We analyzed data from the X-Ray Telescope (XRT) and the Ultraviolet and Optical Telescope (UVOT) on board the Neil Gehrels Swift Observatory (Gehrels 2004) and from the Advanced CCD Imaging Spectrometer (ACIS) on board the Chandra X-ray Observatory (Weisskopf et al. 2000). Full details of the observation parameters for Swift and Chandra are given in the Appendix (Table A1 and Table A2, respectively). Swift and Chandra observed comet 46P during three separate periods (hereafter referred to as epochs) between 2018 November 28 and 2019 January 13 UTC. Favorable observation conditions[5] allowed for monitoring of X-ray and optical/UV emission before, at, and after perihelion ($r_h = 1.055$ au between December 12 and 13, 2018), hence taking advantage of the close passage near the Earth ($\Delta = 0.077$ au on December 16). During the entire observation period, 46P remained very close to the solar equatorial plane, with a heliographic latitude between $-2.^{\circ}1$ and $1.^{\circ}6$.

Data for each of the three epochs were processed by applying data-reduction methods that properly handle changes in the observation geometry because of the object's motion. Exposures within the same epoch, which have similar observation geometries, were merged together to increase the signal-to-noise ratio. A summary of the observation parameters and results for the three epochs are given in Table 1.

2.1. Neil Gehrels Swift Observatory—X-Ray Telescope

Swift was pointed at comet 46P for a total of 122 observations (~41 ks) over the three epochs. Because the observatory is not able to track non-sidereal objects, observations were specifically planned to minimize smearing. During each observation, XRT and UVOT recorded data simultaneously.

The XRT (Burrows et al. 2005) is an X-ray imager characterized by a 23.6×23.6 arcmin^2 field of view, an angular resolution (FWHM) of 18 arcsec, and an effective area of 125 cm^2 at 1.5 keV; the imager is designed for rapid follow-up of gamma-ray bursts. The useful passband is 0.2–10 keV, with an energy resolution of 140 eV at 6 keV and a point-source sensitivity of 2×10^{-14} erg cm^{-2} s^{-1} in 10^4 s. The data used in this analysis were acquired in photon-counting mode, allowing for a full imaging (600×602 pixels) and spectroscopic resolution with a time resolution of 2.5 s.

2.1.1. Data Extraction

For the XRT, all data were recorded in event mode; that is, the arrival time and energy of each photon were registered. Image processing based on the observation geometry and comet trajectory required a dedicated analysis approach and consisted of four steps. First, all the coordinates were shifted to position the comet nucleus into the central bin of the map. The position of the comet on the detector was determined using sky coordinates retrieved from JPL Horizons.[6] This step was performed on a single photon level (we applied a coordinate transformation), producing the same effect as a rigid translation of the reconstructed image. Second, because event data include a timestamp for each of the recorded photons, this information was combined with the comet nucleus orbital parameters to trace back the photon position to the position it would have had if it was recorded at the beginning of the observation. The resulting centered and drift-corrected maps were then rotated to show the Sun at the same fixed direction (left in the following figures). A final transformation was applied to have the same scale in terms of linear distance from the nucleus (i.e., km pixel^{-1}). Depending on the changing distance from the observer (Δ), centered, drift-corrected, and rotated maps were stretched into $1{,}000 \times 1{,}000$ pixel maps with a 200 km pixel^{-1} resolution. Similar processing (shift, rotation, and stretch) was applied to the exposure maps. After applying this four-step transformation, single-observation maps within the same epoch were exposure-corrected and finally stacked together with a simple pixel-by-pixel summation. The resulting stacked XRT maps for the three epochs are shown in Figure 1. This approach is similar to that already used by Carter et al. (2012), to which we have added the fourth step to take into account the varying distance of the comet from the observer and to produce maps showing the map-projected linear distance from the nucleus' center rather than the angular distance.

2.1.2. Background Removal

To estimate the background for the XRT observations, we considered a radial profile of the X-ray emissions with respect to this position. The region around the nucleus was partitioned into concentric annuli using 50 km steps in radius. The top panel of Figure 2 shows the count rate radial distribution for epoch 1, here considering only events with a pulse invariant (PI) between 30 and 100, corresponding to nominal energies in the range of 0.3–1.0 keV. Count rates in the innermost annuli have high fluctuations because they encompass smaller aperture areas that include a relatively small number of counts, whereas the outer annuli are extracted from the edge of the field of view (FoV), where the effective exposure time decreases rapidly. The blue dashed vertical line in Figure 2 (inner region) corresponds to a radial distance of approximately 210″–230″ (considering a geocentric distance range of 0.133–0.120 au during epoch 1), and the two red dashed vertical lines (outer annulus) correspond to approximately 470″–520″ and 620″–690″ from the comet's

[5] https://ssd.jpl.nasa.gov/horizons.cgi

[6] https://ssd.jpl.nasa.gov/horizons.cgi

Table 1
Observation Parameters and Results

		Epoch1	Epoch2	Epoch3
Swift start date	(UTC)	2018 Nov 28 04:03:28	2018 Dec 13 09:08:43	2019 Jan 12 09:55:12
Swift stop date	(UTC)	2018 Dec 1 04:19:53	2018 Dec 13 15:55:38	2019 Jan 13 07:02:53
RA	(*deg*)	36.51.. 38.53	53.70.. 54.19	129.10.. 130.16
Dec	(*deg*)	−23.31.. −19.54	10.57.. 11.59	59.36.. 59.26
r_h	(au)	1.074.. 1.067	1.055.. 1.055	1.132.. 1.137
Δ	(au)	0.133.. 0.120	0.080.. 0.079	0.184.. 0.190
Elongation	(*deg*)	128.2.. 130.3	151.7.. 152.4	140.7.. 140.6
Phase angle	(*deg*)	46.2.. 44.8	26.2.. 25.7	33.4.. 33.3
XRT exposure	(*s*)	19,828	6933	14,342
Counts([1])		4260	1482	1339
X-ray flux([1])	(10^{-13} (erg cm^{-2} s^{-1}))	11.2 ± 0.8	<27.22([2])	<1.384([3])
Aperture for X-ray flux	(km)	20,000	30,000([2])	40,000([3])
V exposure	(*s*)	2160	1184	9173
V flux	(10^{-9} (erg cm^{-2} s^{-1}))	1.35 ± 0.04	4.64 ± 0.11	0.44 ± 0.02
V magnitude	(*mag*)	8.52 ± 0.04	7.18 ± 0.03	9.74 ± 0.05
Aperture for V flux	(km)	10,000	10,000	10,000
UVW1 exposure	(*s*)	2710	246	3927
OH flux	(10^{-9} (erg cm^{-2} s^{-1}))	8.12 ± 0.08	12.29 ± 0.43	6.36 ± 0.07
Aperture for OH flux	(km)	40,000	30,000	70,000
$\mathbf{Q_{H_2O}}$	(10^{28} molec. s^{-1})	1.16 ± 0.01	1.21 ± 0.04	0.78 ± 0.01
SW bulk speed([4,5])	(km s^{-1})	374 (306.. 445)	401 (395.. 410)	406 (380.. 432)
SW p density([4,5])	(cm^{-3})	5.68 (3.23.. 10.1)	2.87 (2.59.. 3.15)	2.58 (2.08.. 2.98)
$\mathbf{O^{7,8+}/O^{6+}}$([4])		0.14 ± 0.05	0.10 ± 0.03	0.11 ± 0.03
$\mathbf{O^{8+}/O^{6+}}$([4])		0.004 ± 0.003	0.014 ± 0.006	0.006 ± 0.004
$\mathbf{O^{8+}/O^{7+}}$([4])		0.03 ± 0.02	0.16 ± 0.07	0.06 ± 0.05
Chandra start date	(UT)	2018 Dec 03 21:16:05	2018 Dec 13 09:06:52	⋯
RA	(*deg*)	40.94.. 41.07	54.10.. 54.56	⋯
Dec	(*deg*)	−15.52.. −14.98	10.14.. 10.96	⋯
r_h	(au)	1.062.. 1.062	1.055.. 1.055	⋯
Δ	(au)	0.108.. 0.107	0.080.. 0.08	⋯
Elongation	(*deg*)	132.9.. 133.2	151.9.. 152.4	⋯
Phase angle	(*deg*)	42.9.. 42.6	26.1.. 25.6	⋯
ACIS-S exposure	(*s*)	20,450	21,560	⋯
No. of photons([6])		2691	2757	⋯
X-ray flux([6])	(10^{-13} erg cm^{-2} s^{-1})	12.5 ± 4.0	6.9 ± 0.5	⋯

Note. (1) $0.3 < E < 1.0$ keV. (2) 3σ upper limit considering background = 30% of total signal. (3) 3σ upper limit. (4) Data from the Advanced Composition Explorer (ACE) observatory. (5) Data from the Solar and Heliospheric Observatory (SOHO) observatory. Solar wind bulk speed and proton (p) density are given as the average values (outside brackets) and ranges (between brackets). (6) Full chip: $0.3 < E < 1.0$ keV, $8\farcm3 \times 8\farcm3$.

nucleus, respectively. The radial-averaged count rate distribution shows a clear maximum located a few thousand km from the predicted position of the nucleus. The position of this peak, (5840 ± 180)km using a 1-D Gaussian fit, is interpreted as the offset between the nucleus and the center of the X-ray emission (this approach only quantifies the intensity of the offset, while the direction, as explained below, is consistent with the Sun's position). The offset is also evident when overlaying the X-ray contours to the hydroxyl (OH) map (Figure 3). Given the symmetry of the OH emission around the comet's nucleus, we attribute the offset to the collisional depth of the coma for the incoming solar wind ions rather than to the distribution of the neutral gas in the coma.

We then recomputed the radial profile using the same approach but shifting the annuli center toward the Sun along the comet–Sun line by 5,840 km. The results are shown in the bottom panel of Figure 2. The X-ray count profile shows a regular decreasing trend down to a constant level. We used this information to identify the candidate regions for extracting the comet signal ($R < 20{,}000$ km) and the background ($45{,}000 < R < 60{,}000$ km). The estimated background is ∼0.1 *cps,* which is consistent with the soft X-ray background that we computed at the comet position during epoch 1 from the ROSAT all-sky survey[7] using the WebPIMMS v4.11 tool.[8]

This approach proved to be effective for epoch 1 but did not allow for a clear definition of a possible background region within the XRT images of epochs 2 and 3. Comet 46P was closest to the Earth during epoch 2 (∼0.08 au) and, because the XRT only covered $\lesssim$35,000 km, the comet filled the entire FoV. For epoch 3, on the other hand, the FoV spanned ∼100,000 km at the comet, but the radial profile shows a very constant count rate from which it is impossible to identify a clear X-ray excess region with respect to the surrounding background.

[7] https://heasarc.gsfc.nasa.gov/cgi-bin/Tools/xraybg/xraybg.pl
[8] https://heasarc.gsfc.nasa.gov/cgi-bin/Tools/w3pimms/w3pimms.pl

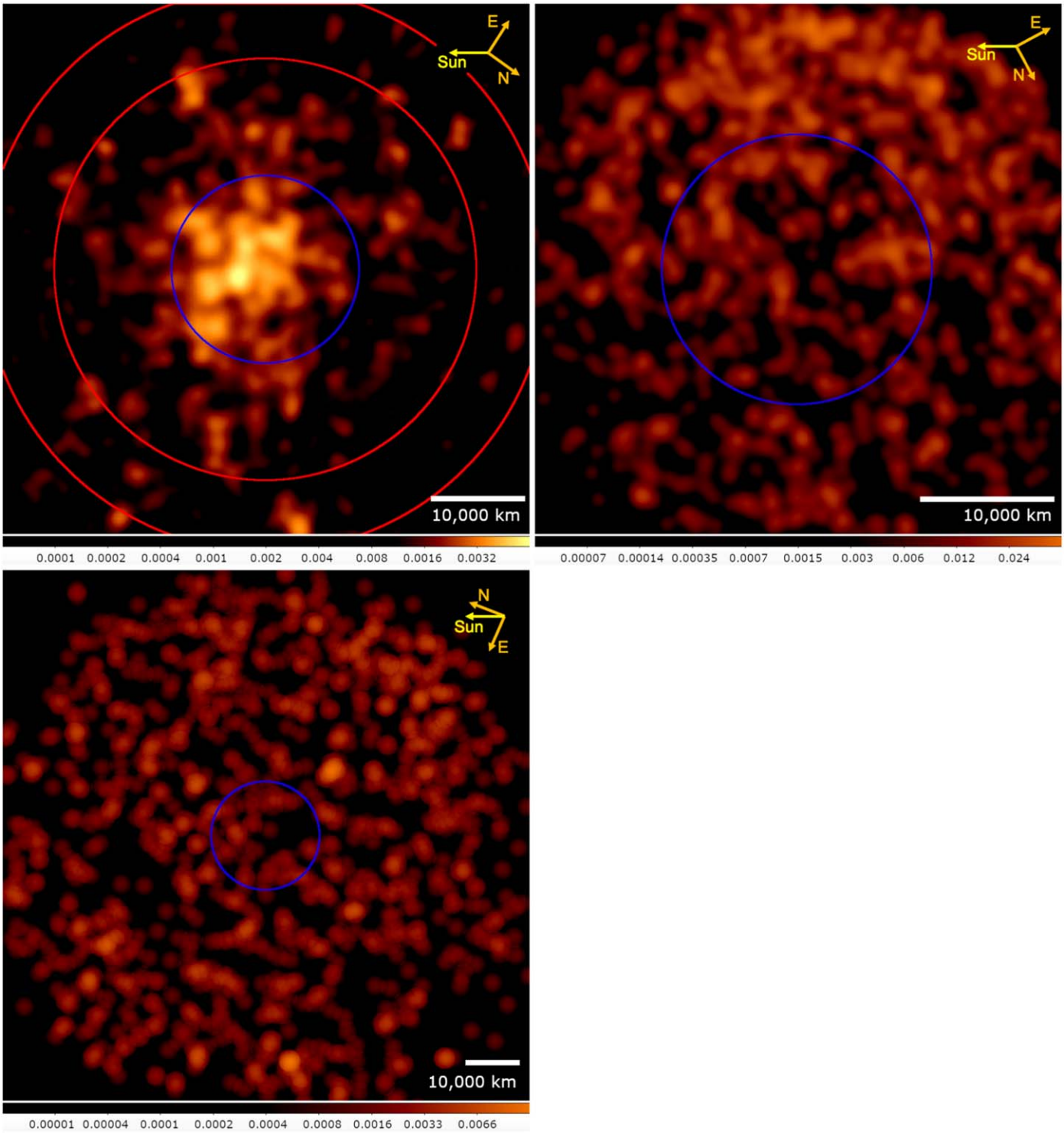

Figure 1. X-ray count maps from Swift/XRT for epoch 1 (top left), epoch 2 (top right), and epoch 3 (bottom). North, east, and Sun direction are indicated by the arrows. The blue circle marks a 20,000 km region centered at the position of the comet's nucleus. The red circles mark the annulus region used for background subtraction (45,000–60,000 km). The reference frame is relative to the first exposure of each epoch (following exposures were rotated to show the Sun on the left). The logarithmic color scale shows the total counts (in arbitrary units after point-spread function (PSF) smoothing).

2.1.3. Spectral Fitting

The background-subtracted spectrum from epoch 1 is shown in Figure 4 and the results are summarized in Table 2. The spectrum was extracted from reduced files (Section 2.1.1) using the above-defined regions. There is a clear excess in the 0.3–1.0 keV energy band (580 ± 30 counts) corresponding to a 20σ detection. A simple empirical three-Gaussian model was fit to the data using the Python interface for the Xspec X-ray spectral fitting package (Arnaud 1996). To limit the number of

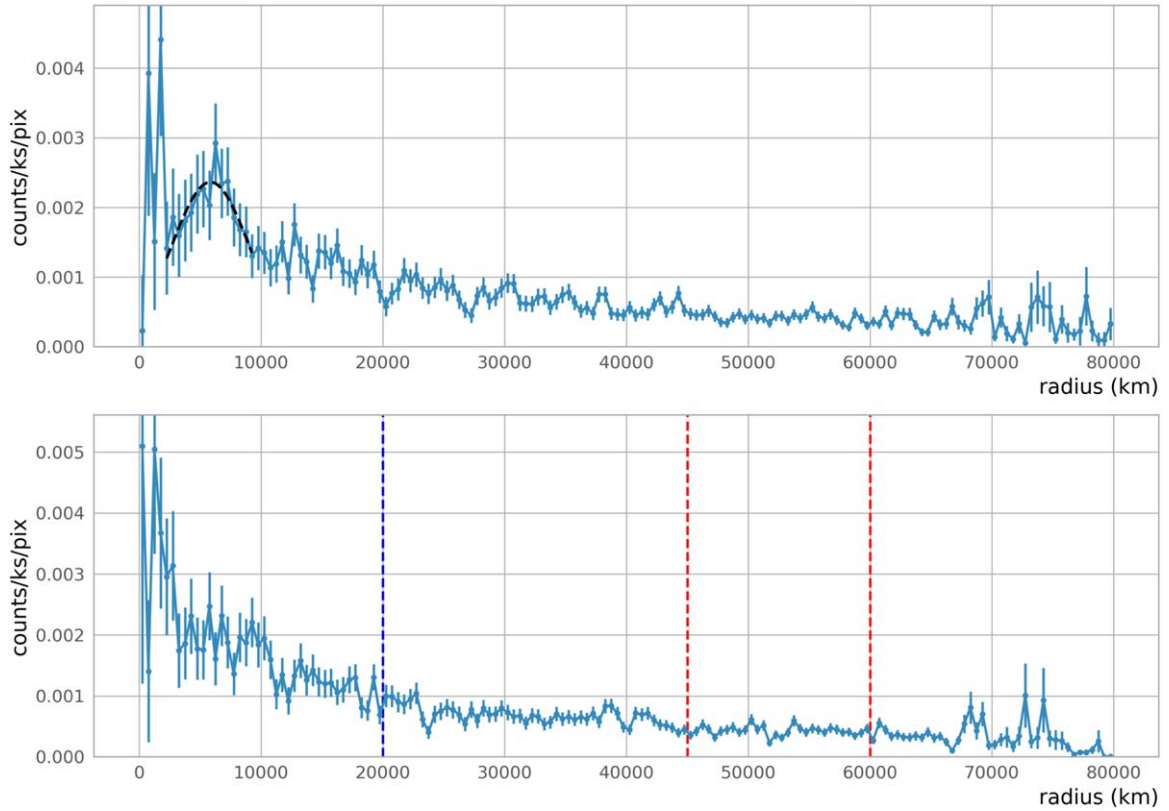

Figure 2. Radial profile of Swift/XRT count rate for epoch 1 before (top panel) and after (bottom panel) offset correction. The black dashed curve in the top panel of the figure shows the Gaussian fit to the X-ray radial profile, indicating the offset between the emission peak and the comet nucleus position. Source (blue dashed vertical line, $R \leqslant 20{,}000$ km) and background (red dashed vertical lines, $45{,}000 \leqslant R \leqslant 60{,}000$ km) regions are also shown in the bottom panel for the offset-corrected radial profile.

degrees of freedom and thus avoid overfitting, the model choice was driven by the instrument's low spectral resolution, following Carter et al. (2012). Gaussian widths were fixed to 1 eV to mimic the signal from monochromatic lines. Single components, however, yield a broader signal in the reconstructed spectrum because of the instrument energy resolution (see red dotted curves in the top panel of Figure 4). Freeing the width parameters degrades the goodness of fit but had no significant impact on the results. The resulting Cash statistic (Cash 1979) for the fit to epoch 1 in the range of 0.3–1.0 keV fit is 44.8 for 57 degrees of freedom. The reduced χ^2 test statistic is 0.674, corresponding to a fit probability of 97.2%. The model flux is $(11.2 \pm 0.8) \times 10^{-13}$ erg cm^{-2} s^{-1}, mean values of the three Gaussians are (0.394 ± 0.008) keV, (0.540 ± 0.004) keV, and (0.675 ± 0.013) keV, respectively. Note that the position of the three line centers shown in Figure 4 are seemingly offset from the energies in Table 2. This offset increases with decreasing energy and is a product of the energy redistribution matrix of the XRT.

During epoch 2, the X-ray emission from the comet filled the XRT's FoV, and it was impossible to use the same approach as epoch 1 for background subtraction. We can estimate a 3σ upper limit on the X-ray flux if we assume the same background level as determined for epoch 1 (i.e., 30%), resulting in 27.22×10^{-13} erg cm^{-2} s^{-1} (see Table 1).

No significant excess was measured in the epoch 3 data when analyzing the inner 40,000 km circle with respect to the outer region up to 100,000 km, and the background-subtracted excess of 17 ± 14 counts is well below the detection threshold of the XRT (Miller et al. 2001). The resulting X-ray spectrum resembles a continuum emission. For comparison purposes, and so as not to introduce bias because of an arbitrary line mixing in the fitting model, we fitted the X-ray emission using a thermal bremsstrahlung model with $kT = 0.23$ keV (Dennerl et al. 1997). The resulting 3σ flux upper limit is 1.38×10^{-13} erg cm^{-2} s^{-1} (see Table 1). The flux upper limit was computed using the WebPIMMS tool and considering a 3σ significance level ($\alpha = 0.135$) and 98% confidence ($\beta = 2\%$; Masci 2011).

2.1.4. Uncertainties

Systematic uncertainty of Swift/XRT ancillary response matrices and energy scale accuracy[9] are in the order of 10% in the 0.5–10 keV energy range (Romano et al. 2005). Such uncertainties include mirror effective area, filter transmission, and the point-spread function (PSF) correction. This uncertainty is found to be of the same order of statistical uncertainties for the flux measurements. A sensitivity analysis of different background regions (closer to the nucleus center, down to 30,000 km) shows a background-subtracted flux reduction up to 30% (epoch 1). The fit model choice only marginally affects the flux estimation. For comparison purposes, power law or thermal bremsstrahlung hypotheses, which return unacceptable fit probabilities (<0.1%), estimate the X-ray fluxes within 2% of the charge exchange model in the 0.3–1.0 keV energy range. Swift's XRT angular resolution is ~18 arcsec, smaller than the typical scale for morphology features observed at epoch 1. A known issue[10] for Swift/XRT

[9] https://www.swift.ac.uk/analysis/xrt/digest_cal.php
[10] https://www.swift.ac.uk/analysis/xrt/optical_loading.php

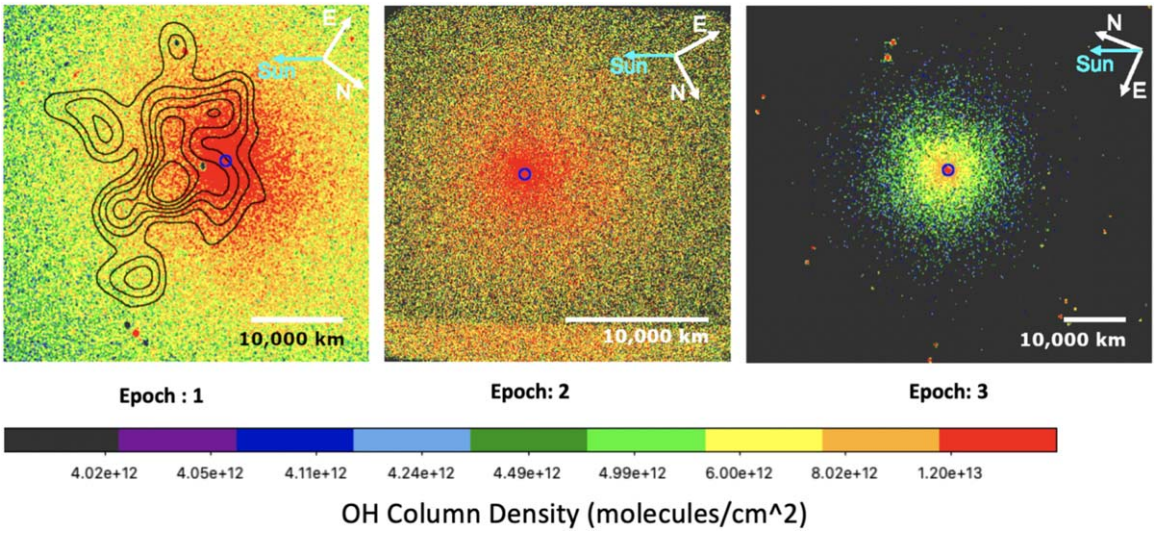

Figure 3. Swift/UVOT OH maps for the three epochs with X-ray contours from Swift/XRT overlaid on epoch 1 (linear steps are used for contours). North, east, and Sun directions are indicated by the arrows. The nominal nucleus position is indicated by a blue circle. For epoch 1, the offset between the X-ray maximum position and nominal nucleus position is (5,840 ± 180) km.

is optical loading, where visible light penetrates the blocking filter, releasing spurious electrons in the charged couple device CCD. Given the low surface brightness of 46P, our observations are not significantly affected by this.

2.2. Neil Gehrels Swift Observatory—UltraViolet-Optical Telescope

Swift's UVOT (Roming et al. 2005) is a 30-cm diameter telescope sensitive to wavelengths between 170 and 600 nm. It is characterized by a 17 × 17 arcmin^2 FoV and a PSF of 0.″9 at 350 nm FWHM. The pixel scale is 0.″5. It is equipped with an 11-position filter wheel that includes six broad-band filters, two grism filters, white and blocking filters, and a magnifier. The data used for this analysis were acquired using the V ($\lambda_c = 544$ nm, FWHM = 75.0 nm) and UVW1 ($\lambda_c = 251$ nm, FWHM = 70.0 nm) filters.

2.2.1. Data Extraction

For the UVOT, "event mode" was used for only half of the data for every epoch because telemetry limitations prevented us from acquiring all data in event mode. The other data used "image mode", where information about single photons is not available. To compensate for the comet motion during fixed-pointing exposures, we used only event-mode data to derive motion-corrected images and did further reductions for epoch 1 and epoch 2, which were very smeared by the comet motion (∼5 arcmin h^{-1} for epoch 1 and 10 arcmin h^{-1} for epoch 2). For epoch 3, which was much less affected by smearing (motion ∼2.4 arcmin h^{-1}), we used both event-mode and image-mode data for data reduction without motion correction. For every epoch, the remaining individual exposures were aligned and co-added to increase the signal-to-noise ratio. Because of the high surface brightness of 46P during our observations, a rough coincidence loss correction was applied to the co-added V and UVW1 images (Poole et al. 2008; K. Venkataramani et al. 2022, in preparation). The resulting stacked UVOT maps for the three epochs are shown in Figure 3.

2.2.2. Background Subtraction

The close (and small) FoV hobbles the background estimation; thus, we assumed that all epochs have the same UV background as epoch 3, which has the largest FoV (∼70,000 km). To measure the background brightness for epoch 3, we obtained the surface brightness at 70,000 km from the position of the nucleus in the co-added OH image. Although the FoV of epoch 3 spans the largest area at the comet, it is still small compared with the coma, and the light from the coma still contributes significantly to the surface brightness. To exclude this contribution, we compared the surface brightness of the coma of 46P at 70,000 km for Swift observations of comet C/2009 P1, which has a much lager FoV. We found that about 85% (UVW1 filter) or 75% (V filter) of the brightness at 70,000 km is contributed by the coma, so we corrected it to obtain the final background brightness.

2.2.3. Water-Production Rates

OH is a product of H_2O photolysis in the coma, and its fluorescent emission is commonly used to determine the water-production rates of comets (cf. A'Hearn et al. 1995). Fluorescence emission of the OH $A\,^2\Sigma^+ - X\,^2\Pi$ band between 280 and 330 nm is covered in the bandpass of the UVW1-filter of Swift/UVOT, which was used to map the OH coma in our observations. To remove the contribution of sunlight reflected by dust to the UVW1 maps, we use contemporaneous V-band observations (Table A1). We subtracted the co-added, background-removed V-filter images from the UVW1-filter images weighted by a continuum removal factor of 0.0928 to obtain pure OH images, assuming that the comet's dust has the same color as the Sun. Figure 3 shows the OH images of the three epochs.

To determine the total count rates, we masked the regions on the detector that contain significant reflection from part of the detector housing (Breeveld et al. 2010). We then derived the azimuthal median surface brightness profiles from the masked OH images to remove the contribution from background stars, and integrated the profiles to obtain the total count rates (Bodewits et al. 2014). To adapt to the differences in the observing geometry, we used apertures with different radii for

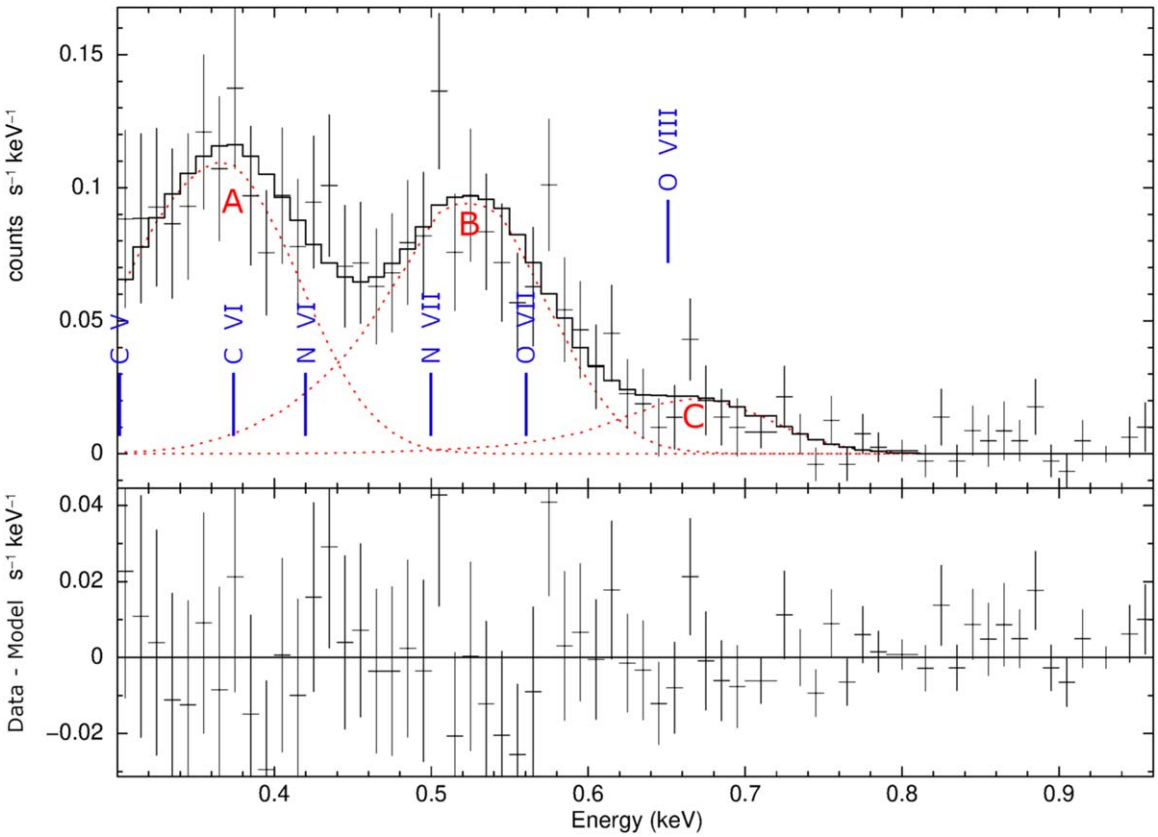

Figure 4. Swift/XRT background-subtracted spectrum for epoch 1 (top panel) and fit residuals (bottom panel). Error bars show 1σ relative errors. In the top panel of the figure, the modeled fitted spectrum (solid black curve) consists of three Gaussian components (red dotted curves A, B, and C, and the position of the most prominent known solar wind charge-exchange emission features are indicated with blue vertical lines in the top panel (Bodewits et al. 2007)).

Table 2
Swift/XRT Spectral Fitting Results for Epoch 1

Line ID	Attribution	Energy (eV)	Line Flux[a]
A	C VI Ly-α	394 ± 8	6.9 ± 0.7
B	O VII f + r + i	540 ± 4	7.1 ± 0.9
C	O VIII Ly-α	675 ± 13	0.7 ± 0.2
	$\widetilde{\chi}^2$	0.7	
	Observed flux[b]	11.2 ± 0.8	

Notes.
[a] Line flux in units of 10^{-4} ph cm^{-2} s^{-1}.
[b] Observed flux is in units of 10^{-13} erg cm^{-2} s^{-1}.

the three epochs (epoch 1: 40,000 km; epoch 2: 30,000 km; and epoch 3: 70,000 km). We also excluded the central regions with a 50 pixel aperture for all epochs to reduce the effects of coincidence loss, comet motion, and the PSF. The total count rates were then linearly converted to the total number of OH molecules by using heliocentric velocity-dependent fluorescence efficiencies (Schleicher & A'Hearn 1988). For every epoch, we derived the production rate of OH and H_2O molecules using the vectorial model[11] within the same aperture, the central region of which was also excluded as described above for the comet images. For this we assumed lifetimes of 8.6×10^4 s for H_2O and 1.29×10^5 s for OH at a distance of 1 au from the Sun, a bulk velocity of $0.85 \times r_h^{-2}$ km s^{-1} (where r_h is in au), and a constant OH velocity of 1.05 km s^{-1}. Water-production rates (Q_{H_2O}) were finally scaled by the ratio of the measured and modeled number of OH molecules, and the results are $(1.16 \pm 0.01) \times 10^{28}$ molec. s^{-1} for epoch 1, $(1.21 \pm 0.04) \times 10^{28}$ molec. s^{-1} for epoch 2, and $(0.78 \pm 0.01) \times 10^{28}$ molec. s^{-1} for epoch 3, respectively, where all errors are 1σ stochastic errors.

[11] Web Vectorial Model: https://www.boulder.swri.edu/wvm/.

2.2.4. Uncertainties

The spatial resolution of Swift/UVOT is 0.5 arcsec/pixel for event-mode data and 1.0 arcsec/pixel for image-mode data. The sensitivity of Swift/UVOT was initially calibrated with an accuracy of 4% (Poole et al. 2008). However, its calibration has not been recently updated, and its sensitivity was reported to be decreasing at a rate of 1% per year (Breeveld et al. 2011), which can lead to an underestimation of ~10%. Modeling uncertainties for the gas density distribution around the comet nucleus are as high as 25% (Bodewits et al. 2014), and measurements of water-production rates show a short-time variability of up to 20% (Bonev et al. 2021). The resulting uncertainty on a single measurement of Q_{H_2O} can be as high as 40% of the nominal value.

2.3. Chandra X-ray Observatory—Advanced CCD Imaging Spectrometer

Chandra's ACIS (Garmire et al. 2003) consists of a 2×2 array of front-illuminated CCDs designed for imaging (ACIS-I) and a strip of six CCDs to be used with gratings for

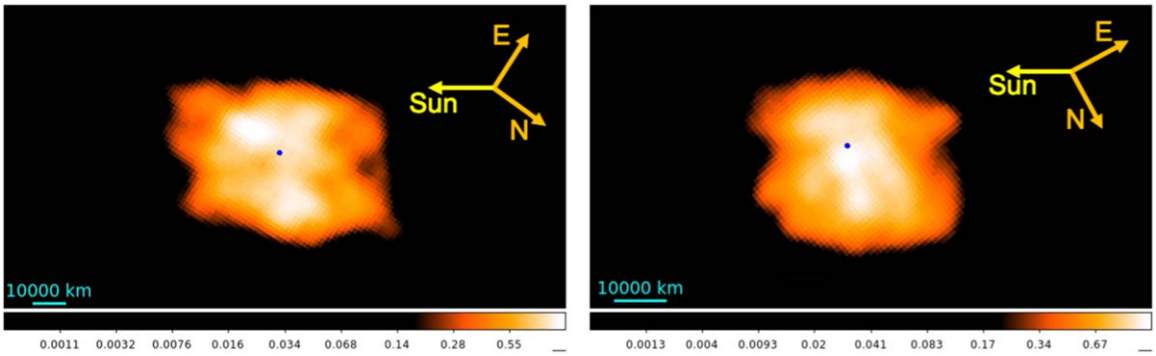

Figure 5. Chandra/ACIS-S3 images in the 0.3–0.8 keV energy range for comet 46P. The left panel shows the ACIS-S3 image for epoch 1 (Dec 3); the right panel shows the ACIS-S3 image for epoch 2 (Dec 13) (logarithmic stretch). North, east, and Sun direction are indicated by the arrows. The nominal nucleus position is indicated with a blue circle along with a scale in both images.

spectroscopy (ACIS-S). Each CCD has a 8.4×8.4 arcmin^2 FoV. The energy resolution of the ACIS-S chips is $\sim$110 eV (0.25–0.8 keV; Lisse et al. 2001), with a PSF of 2 arcsec (90% containment radius). The sensitivity to point sources is 4×10^{-15} erg cm^{-2} s^{-1}. Because of the molecular contamination of the optical blocking filter (Plucinsky et al. 2016), the soft X-ray effective area has degraded significantly and has become comparable with that of Swift/XRT.

Chandra acquired 14 observations of comet 46P during two separate periods, which are close in time to the first two epochs defined for Swift (Chandra epoch 1 started 2.7 days after the end of Swift epoch 1, while epoch 2 was coincident; see Table A2). Dedicated background observations (10 ks blank-sky pointings) were performed at the beginning and end of each epoch according to the detailed observation log shown in A2. This strategy proved to be critical for the successful detection of X-ray emissions, as described in Section 4 (Christian et al. 2010).

The observation strategy was similar to previous comet observations with Chandra, where the comet was centered in the ACIS-S3 chip and then allowed to drift and the pointing updated following the comet ephemeris (i.e., drift-scan).

2.3.1. Data Extraction

Data were reduced with the Chandra Interactive Analysis of Observations (CIAO version 4.11) software (Fruscione et al. 2006). The built-in routine sso_freeze was applied to project the photon position according to the nucleus drift. Comet spectra were extracted for the full ACIS-S3 chip and several select regions before being analyzed with a combination of CIAO and custom interactive data language (IDL) software. CIAO also generated associated calibration products (response matrices and effective areas) for each comet epoch. Background spectra were extracted from the full ACIS-S3 chip for the combined pointings of December 3 and 4 for Chandra X-ray Observatory (CXO) images of epoch 1 and the two December 13 pointings for epoch 2 6. The signal of the comet is about 6σ above the background in both epochs. The signal of the comet does not exceed that of the background above $\sim$1.25 keV. No contaminating point sources were found in either the comet or background pointings. These exposure times are also given in Table A2. Because of the relative faintness of 46P, in the current paper we concentrate on the 0.3 to 1 keV region and investigate the expected emission lines predicted by solar wind charge exchange models. Intensity maps for epochs 1 and 2 are shown in Figure 5, showing excess emissions near the nominal cometary nucleus positions.

2.3.2. Spectral Fitting

Although comet 46P did not show the image morphology of brighter, more active comets, several X-ray emission features were detected above the background level in the 0.3–0.4 and 0.5–0.7 keV regions in both epoch 1's and epoch 2's spectra (see Figures 6 and 7). ACIS-S3's background-subtracted spectra (extracted from the full ACIS-S3 chip) were fitted with a simple multi-emission line model (with six lines) to mimic solar wind charge exchange with cometary neutrals. The moderate signal-to-noise spectra did not merit being fitted with more sophisticated models (such as in Bodewits et al. 2007; Cumbee et al. 2018). The X-ray spectral analysis software package Xspec was used for the spectral fitting (Arnaud 1996).

The two spectra were fit with a six emission line model, and these results are presented in Table 3. The energy of these lines was generally fixed to the charge exchange model by Bodewits et al. (2007) but was allowed to vary for features E and F in both epochs (attributed to Ne IX and Ne X, and for features C and D, attributed to O VII and O VIII, in epoch 2). The uncertainty of the positions of these lines is approximately 30 eV. Both epoch 1's and epoch 2's spectra had emission lines near 0.3, 0.5, 0.56, 0.65, 0.8–0.9 keV, and 1.04–1.1 keV. Epoch 2 showed little emission near 0.56 keV but had an additional emission line near 0.69 keV that we attributed to O VIII Lyα.

2.3.3. Uncertainties

Calibration uncertainties on the Chandra/ACIS effective area are in the order of 4%[12] and up to $\sim$10% in the 0.5–2.0 keV energy band from cross-calibration studies (Nevalainen et al. 2010). This value is smaller than or comparable to flux uncertainties from epochs 1 and 2. Although CXO images of epoch 1's and epoch 2's spectra are near the detection threshold for Chandra, we find excess emission at line energies for the charge-exchange models. We also note the large line fluxes found for emission features near 300 eV, which we attribute to C V. We note this part of the ACIS-S spectra is difficult to model because of the large loss of effective area from the carbon edge near 284 eV and the rising background. Similar large C V fluxes at $\sim$300 eV have been found in all Chandra studies of comets (e.g., Christian et al. 2010 for 8P/Tuttle; Lisse et al. 2013 for 103P/Hartley.). Recently, Snios et al. (2016) found excess emission at $\sim$200 eV for comet C/2012

[12] https://cxc.cfa.harvard.edu/cal/summary/Calibration_Status_Report.html

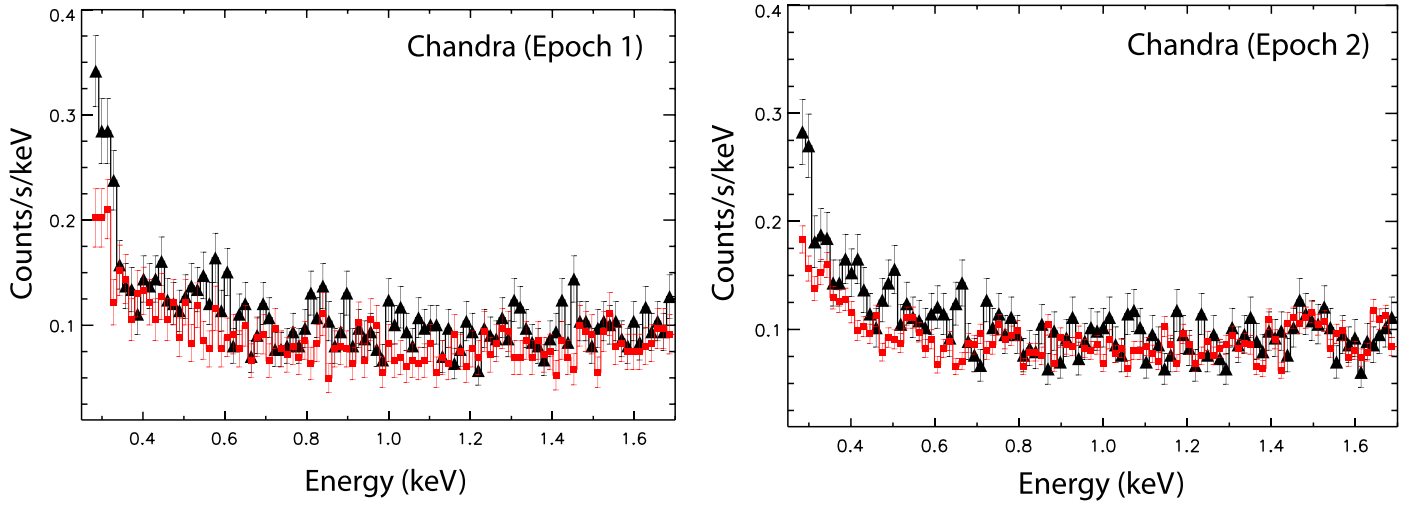

Figure 6. Chandra/ACIS-S3 spectra of comet 46P for epoch 1 (left panel) and epoch 2 (right panel). Black triangles indicate raw counts (comet + background), and red squares indicate the background signal. While there is a faint detection at low energies, above 1.2 keV, the X-ray signal from the comet does not exceed that of the background.

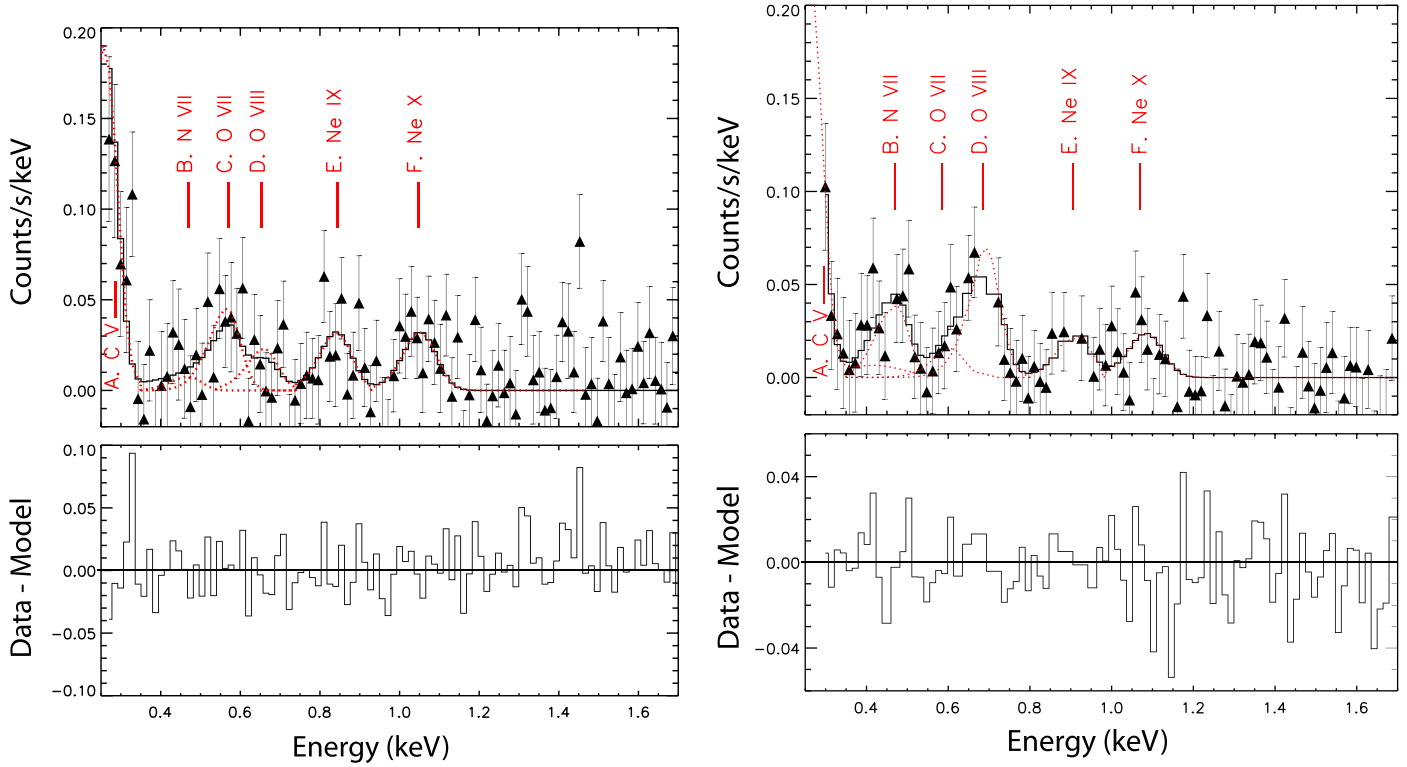

Figure 7. Chandra/ACIS-S3 spectra of comet 46P for epoch 1 (left panel) and epoch 2 (right panel). Each figure shows the background-subtracted spectrum over-plotted with the best fitting emission line model with the residuals (model subtracted from the data) shown below. The model consists of six Gaussian components for both epochs 1 and 2. Individual Gaussian components are over-plotted in each panel as red dotted lines, and line IDs are indicated.

S1 (ISON) in their ACIS spectra and confirmed it with simultaneous High Resolution Camera (HRC) imaging.

2.4. Heliospheric Charge Exchange Background

Charge exchange reactions with neutral hydrogen and helium in the interplanetary space produce an additional background component that depends on solar wind parameters, as well as the look direction through the three epochs. When the background is extracted from regions of the same FoV as the comet (as is the case for Swift epoch 1), this component is effectively subtracted. However, in the remaining Swift observations (epochs 2 and 3), this strategy could not be applied, and any changes in the heliospheric component between the three epochs need to be accounted for. In addition, for Chandra, although performing background observations just before and after the comet observations should minimize the effect, some variability of the heliospheric signal cannot be excluded.

We have estimated the variability of the heliospheric component by calculating the O VII triplet emission based on

Table 3
Chandra/ACIS-S Spectral Fitting Results

Line ID	Attribution	Epoch 1		Epoch 2	
		Energy (eV)	**Line Flux**[a]	**Energy** (eV)	**Line Flux**[a]
A	C V f + r + i	300[b]	17 ± 4	300[b]	20 ± 8
B	N VII Ly-α	470	0.9 ± 0.5	470	5 ± 3
C	O VII f + r + i	561	8 ± 2	580	1.1 ± 0.7
D	O VIII Ly-α	653	0.8 ± 0.4	686	1.7 ± 0.4
E	Ne IX f + r + i	838	0.3 ± 0.1	905	0.2 ± 0.1
F	Ne X	1048	0.14 ± 0.05	1078	0.1 ± 0.06
	$\widetilde{\chi}^2$	0.8		0.5	
	Observed flux[c]	12.5		6.9	

Notes.
[a] Line flux in units of 10^{-4} ph cm^{-2} s^{-1}.
[b] Line width of 70 eV.
[c] Observed flux is in units of 10^{-13} erg cm^{-2} s^{-1}.

heliospheric charge exchange models (Koutroumpa et al. 2006; Koutroumpa 2012) and empirical formulas of the O^{7+} flux as a function of the ACE/Solar Wind Ion Composition Spectrometer (SWICS) O^{7+}/O^{6+} data (Kaaret et al. 2020). We find that the O VII triplet line flux has a maximum variation of a factor of 2 between the Chandra epoch 1, which yields 1.4 LU (line units = ph cm^{-2} s^{-1} sr^{-1}) for both the background and comet exposures, and Swift epoch 3, which yields 0.7 LU. The remaining epochs yield a heliospheric O VII line flux of approximately 1.0 LU, with no difference between the background and comet exposures in Chandra/ACIS epoch 2. This is approximately 3.4 times lower than for typical slow solar wind conditions at low latitudes based on Schwadron and Cravens' (2000) abundances, because of the strong depletion of O^{7+} ions during the current solar cycle phase. Assuming the Schwadron and Cravens (2000) relative ion abundance distributions, here scaled to the computed O VII triplet emission, we estimate the total heliospheric emission in the 0.3–1.0 keV energy range to be 6.9 ± 1.4 LU for the period including the three epochs. This amounts to approximately $22 \pm 8\%$ of the total diffuse background (including galactic disk+halo emission and extragalactic sources) at low ecliptic latitudes for the same period based on recent studies with the HaloSat cubesat mission (Ringuette et al., personal communication/in preparation).

2.5. Space Weather Conditions

Given the proximity and similar heliographic latitude of comet 46P to Earth, we can use solar wind measurements acquired by the ACE and the SOHO at L1 and compare these with the Swift and Chandra results. To extrapolate the time of arrival from L1 to the comet's position, a radial plus corotational time shift was calculated according to Neugebauer et al. (2000). Data from the SWICS (Gloeckler et al. 1998; bulk velocity of alpha particles, oxygen charge state distribution) and the Solar Wind Electron Proton Alpha Monitor (SWEPAM; McComas et al. 1998; proton density) onboard the ACE spacecraft were used to estimate space weather parameters at the comet position (see Figure 8). Data from the Charge, Element, and Isotope Analysis System (CELIAS) on board SOHO (Hovestadt et al. 1995) were used to fill some gaps in the ACE data set (i.e., n_p for epoch 3 was not available because of a detector malfunction, so we used measurements of the bulk alpha particle velocities instead).

Figure 8 shows the variation of relevant solar wind parameters and the corresponding observation epochs. In particular, we used 2 hr averaged values for proton density (n_p), helium nuclei velocity ($v_{He^{++}}$), and O^{8+}/O^{6+} and O^{7+}/O^{6+} ratios (from which O^{8+}/O^{7+} and $O^{7,8+}/O^{6+}$ were derived).

3. Results

In this section, we discuss the results from the Swift and Chandra observations of comet 46P in the three epochs. The results from epoch 1 are discussed in Section 3.1 and the results from epoch 2 in Section 3.2. Epoch 3 was only observed by Swift, and the results are discussed in Section 3.3. The X-ray emission comparison and a study of the factors responsible for its variability are discussed in Section 4.

3.1. Epoch 1: 2018 November 28 to 2018 December 3

3.1.1. Neil Gehrels Swift Observatory

The detection during epoch 1 provided the highest signal-to-noise ratio of all three epochs (20σ in the 0.3–1.0 keV band). The measured flux in the $0.3 < E < 1.0$ keV energy range is $(11.2 \pm 0.8) \times 10^{-13}$erg cm^{-2}s^{-1}, corresponding to an X-ray luminosity $L_X = (5.0 \pm 0.4) \times 10^{13}$ erg s^{-1}.

The morphology of 46P observed by Swift/XRT during epoch 1 shows no evidence of a large-scale crescent-shaped morphology, but we observed a peak brightness located approximately 6,000 km from the position of the nucleus toward the Sun's direction (see Figures 3 and 2), corresponding to 8,000 km when corrected for the foreshortening caused by the phase angle of 46°. The presence of a crescent-shape morphology, as was seen in comet C/1996 B2 (Hyakutake; Lisse et al. 1996), depends on both the gas-production rate of a comet and the phase angle under which it is observed. At very low phase angles, even a very active comet would likely appear as a spherical object in X-rays. This indicates that most of the coma is collisionally thin for radial distances outside 6,000 km, which is consistent with other observations of other comets with comparably low water-production rates around 10^{28} molec. s^{-1} (e.g., Lisse et al. 2001).

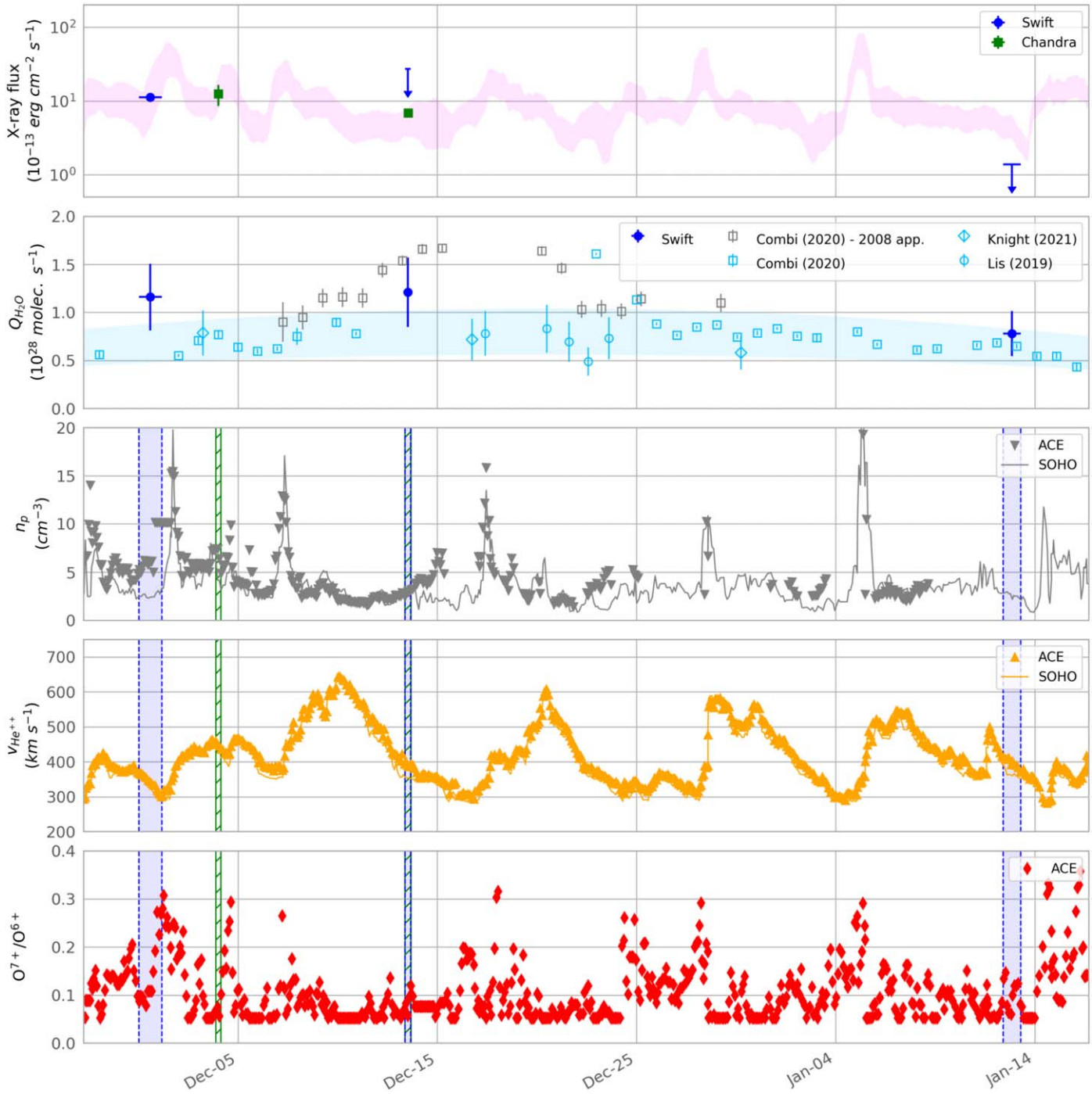

Figure 8. Comparison of the X-ray and optical/UV results from Swift (blue) and Chandra (green) with time-shifted solar wind properties as measured by ACE and SOHO. The three Swift epochs are marked by vertical blue-shaded regions in panels c, d, and e. The green dashed regions show the two Chandra epochs (Swift epoch 2 is coincident with Chandra epoch 2). In the plot, epoch 1 is shown starting from 2018 November 30 00:42:06 UTC because, prior to that date, the exposure accounted for less than 6% the total exposure time (see Table A1). Panel (a) shows the observed X-ray flux (1σ relative errors). The shaded region is the expected X-ray flux from charge exchange-induced emission (arbitrary units, comet distance from the observer taken into account). Panel (b) shows the water-production rate. Swift/UVOT Q_{H_2O} measurements (blue) include the 40% uncertainty, as discussed in Section 2.2.4. SOHO observations of Q_{H_2O} derived from hydrogen Lyα observations for the 2018 (cyan squares) and the 2008 apparitions (gray squares) are from Combi et al. (2019a); Stratospheric Observatory for Infrared Astronomy (SOFIA) measurements of H_2O from Lis et al. (2019) are indicated by cyan circles; and production rates derived from OH observations using the telescopes at Lowell Observatory are indicated by cyan diamonds (Knight et al. 2021). Horizontal error bars on Swift and Chandra (not visible) results represent the epoch time span according to vertical bars in panels (c), (d), and (e). Panel (c) shows ACE/SWEPAM and SOHO/CELIAS measurements of n_p. Panel (d) shows ACE/SWICS and SOHO/CELIAS measurements of $v_{He^{++}}$. Panel (e) shows ACE/SWICS measurements of O^{7+}/O^{6+}). Variability in the estimation of X-ray flux in panel (a), caused by different values for n_p and $v_{He^{++}}$ by ACE and SOHO, are included together with uncertainties in the measurements of the water-production rate. The shaded area in the second panel from the top shows the smoothed trend for Q_{H_2O}, including the two apparitions of 2018 and 2008 (properly time-shifted to match the 2018 perihelion).

This offset is smaller than the offset observed for comet C/2007 N3 (Lulin; 35,000 km, corresponding to 37,000 km after correcting for foreshortening at a phase angle of 75°; Carter et al. 2012). Based on Swift/UVOT measurements, Carter et al. (2012) reported an OH production rate of 5.5×10^{28} molec. s^{-1} for C/2007 N3, compared to our water-production rate of 1.16×10^{28} molec. s^{-1} for 46P (see Section 2.2.3). We note that this offset is proportional to the difference in the water-production rates between the two comets. We attribute the offset location of the brightness maximum to the coma becoming collisionally thick to charge exchange as neutral gas densities increase gradually while approaching the nucleus rather than caused by a local enhancement in the coma further away from the nucleus (through jets or extended sources; Lisse et al. 2005). We favor this interpretation because the maximum falls on the comet–Sun axis, because it scales with the production rate compared with the X-ray offsets observed in other comets, and because there is only one X-ray feature visible (instead of a brightness maximum at the position of the nucleus and one in the coma, as was the case for 2P/Encke Lisse et al. 2005).

The background-subtracted spectrum from epoch 1 is shown in Figure 4, and the results are summarized in Table 2. The simplified three-Gaussian model provides a good fit to the observed spectrum. Our model takes possible blended lines into account, and because of the instrument's line spread function (LSF), such lines are observed as a single broad Gaussian-like component in the X-ray spectrum. Based on the fit results (see Table 2 and Figure 4), the component position (μ parameter of the Gaussian distribution) can be associated to charge-exchange emission lines from specific ions. The first component (centered at 0.394 keV) is consistent with C VI$_{Ly\alpha}$ (0.368 keV) and N VI$_{f+r+i}$ (0.420–0.431 keV) lines, the second (0.540 keV) with O VII$_{f+r+i}$ (0.561–0.574 keV), and the third (0.675 keV) with O VIII$_{Ly\alpha}$ (0.654 keV) (Christian et al. 2010; see Figure 4). Possible contributions from C V$_{f+r+i}$ (0.299–0.308 keV) and N VII$_{Ly_\alpha}$ (0.500 keV) would be expected at the low energy boundary and between components 1 and 2, respectively. Adding additional components to the model, however, does not improve the goodness of fit.

We assumed that the second and third Gaussian components of the fit in Figure 4 are predominantly caused by charge-exchange emission from solar wind oxygen ions (namely O^{7+} and O^{8+}). One would expect a contribution of O VII in the third component at 675 eV by the $1s3p$-$1s^2$, $1s4p$-$1s^2$, $1s5p$-$1s^2$, and $1s6p$-$1s^2$ transitions (Bodewits et al. 2007). To compute how many counts from O VII would be expected in the second and third components, respectively, we assumed a solar wind bulk velocity of 400 km s^{-1} and used the emission cross-section for each transition from O VII (Bodewits et al. 2007).

Based on these emission cross-sections, the ratio between O VII emission around 560 eV and that from the transitions from higher states emitting between 650 and 730 eV is 0.063. Thus, we would expect the contribution of O VII to the flux in peak C to be 0.063 times the flux in peak B. This O VII contribution corresponds to approximately 66% of the total flux in peak C; the rest of the flux is attributed to O VIII. Using the emission cross-sections for O VII and O VIII, these corrected fluxes can then be used to estimate the ratio between the abundance of O^{8+} and O^{7+} ions in the solar wind, for which we find 0.04 ± 0.13. According to ACE/SWICS data, the solar wind had a O^{8+}/O^{7+} ratio of (0.03 ± 0.02) during epoch 1 (Table 1), which agrees with our results. As indicated in Figure 4, peak B likely contains N VII emission, likely at the 10% level based on the Chandra observations during epoch 1 (cf. Section 3.1.2). This implies that the Swift-derived ion ratio is a slight underestimate. We note that both the solar wind flux and the $O^{7,8+}/O^{6+}$ ratio (i.e., the oxygen ions that can produce X-rays) were larger during epoch 1 than during the other two epochs.

The high uncertainty in the solar wind estimate from the X-ray spectrum is because of two factors. First, the spectrum above 0.62 keV (the peak value of the third Gaussian component in Figure 4) is characterized by a low count yield (the signal-to-noise ratio is 8), and this produces large uncertainties in the corresponding X-ray flux. Second, the variation is intrinsic to the solar wind properties as the ACE/SWICS measurement of the O^{8+}/O^{7+} ratio for epoch 1 has a relative error of approximately 80%.

3.1.2. Chandra X-ray Observatory

The Chandra/ACIS spectrum for epoch 1 (acquired some 2.5 days after the end of the Swift observations) was fitted with six emission lines at 0.300, 0.470, 0.561, 0.653, 0.835, and 1.047 keV (see Figure 7). We attribute these to C V, C VI+N VI +N VII, O VII, O VIII, and Ne IX + Ne X, respectively. The observed Chandra flux is $(12.5 \pm 4.0) \times 10^{-13}$ erg $cm^{-2}s^{-1}$, which is similar to the flux measured by Swift/XRT during its observations in epoch 1 (see Table 2). This corresponds to an X-ray luminosity of $L_X = (4.3 \pm 1.3) \times 10^{13}$ erg s^{-1}. The Chandra epoch 1 spectrum shows a modest signal for the O VIII line at 653 eV and after correcting for ~10% O VII contamination and accounting for the emission cross-sections, we find a O^{8+}/O^{7+} ratio of 0.05 ± 0.08.

3.1.3. Comparison with Solar Wind Observatories

We also analyzed O^{7+}/O^{6+} and C^{6+}/C^{5+} ratios during epoch 1 to identify the solar wind state according to Lepri et al. (2013). The ACE/SWICS measurements for epoch 1 are $O^{7+}/O^{6+} = 0.14 \pm 0.05$ and $C^{6+}/C^{5+} = 1.0 \pm 0.3$, respectively, consistent with the slow solar wind properties at solar minimum. No interplanetary coronal mass ejection (ICME) was observed within the time frame of this study.[13] To avoid the chance of an undetected ICME, we used the approach presented in Richardson and Cane (2010), where the O^{7+}/O^{6+} ratio can be used to identify ICMEs. We find that, for epoch 1, even if O^{7+}/O^{6+} is at the higher boundary for a slow solar wind state, it is still lower than the typical values for ICMEs. Finally, one stream interaction region (SIR) was observed close to epoch 1 by the Parker Solar Probe first and STEREO-A later (Allen et al. 2020). Its detection at the STEREO-A location on December 1 places it outside of our observation window, as the time shift (radial plus corotational) is ~4 days. We can conclude that comet 46P interacted with a typical slow solar wind state during epoch 1.

According to ACE and SOHO, the space weather during Chandra epoch 1 was comparable to that during Swift epoch 1. The SOHO and ACE results indicate that, during the Chandra observations, the solar wind was faster (460 ± 10 km s^{-1}) than during the Swift observations (on average 334 ± 23 km s^{-1}), while proton densities were comparable during the two observations. The O^{7+}/O^{6+}, O^{8+}/O^{6+}, and C^{6+}/C^{5+} ratios

[13] http://www.srl.caltech.edu/ACE/ASC/DATA/level3/icmetable2.htm

were all approximately two times higher during the Swift observations than during the Chandra observations. This overall lower charge state distribution explains why there is a strong C VI 380 eV peak in the Swift observations that has changed into a C V peak in the Chandra spectrum. During epoch 1, the two satellite-measured total X-ray fluxes were nearly identical despite the lower charge state distribution. It is likely that the 30% solar wind velocity increase during the Chandra observations compensated for the decrease in the ionization state of oxygen and carbon in the solar wind.

3.2. Epoch 2: 2018 December 13

3.2.1. Neil Gehrels Swift Observatory

There is no clear morphological evidence for the comet in the XRT epoch 2 observations and the count rate profile appears to be constant within the entire aperture. This could depend either on the lack of X-ray signal from the comet or because the comet fills the entire FoV (the FoV for epoch 2 is $\lesssim$35,000 km, while the background region for epoch 1 was identified between 45,000 and 60,000 km, as shown in Figure 1). We tried to include an analytic X-ray background model in the spectral fit, which was unsuccessful because of the combination of limited spectral resolution and the increase of additional free parameters resulting in overfitting of the data. Instead, we looked for background measurements of the same sky position from different, archival campaigns.

The Swift archive includes two blank-sky observations at the position of the comet during the second epoch[14] for a total of 1,558 s exposure, but they were taken ~4–5 yr before our observations. Solar wind parameters vary over different timescales from long-term solar cycle variations (~11 years) to impulsive variations (e.g., coronal mass ejections and co-rotating interaction regions) that occur on timescales as short as a few hours (cf. Section 4.1). Consequently, not only the average background X-ray flux from charge exchange-induced emission can be generally different, but also the spectral features, which depend on the ionic ratios in the solar wind. Therefore, these observations are likely not representative of the space weather conditions during epoch 2.

When we do use these archival observations for background subtraction, however, a O^{8+}/O^{7+} ratio of 0.22 ± 0.12 is obtained, consistent with the ACE/SWICS measurements for the same epoch (0.16 ± 0.07), suggesting the presence of detectable charge-exchange emissions. A detailed analysis of these data, however, could not be performed because of the absence of a reliable X-ray background measurement.

To establish a measure of the upper limit of the comet's X-ray flux, we assumed the same relative background contribution as during epoch 1 (i.e., $30 \pm 9\%$). This results in a flux within the 0.3–1.0 keV energy range of less than 27.2×10^{-13} erg cm^{-2} s^{-1}, corresponding to $L_X < 4.8 \times 10^{13}$ erg s^{-1}. Such an upper limit is consistent with the values measured during Swift epoch 1, suggesting a lower X-ray luminosity during epoch 2, as confirmed by Chandra (cf. Section 3.2.2). This is also supported by the measured water-production rate for epoch 2, $Q_{OH} = (1.21 \pm 0.04) \times 10^{28}$ molec. s^{-1}, which is similar to that measured during epoch 1; i.e., $(1.16 \pm 0.01) \times 10^{28}$ molec. s^{-1}.

[14] Obs_id 00055024 (2014-01-23 03:30:01) and Obs_id 00059030 (2015-01-24 04:19:07).

3.2.2. Chandra X-ray Observatory

The Chandra epoch 2 spectrum was fitted with six emission lines, and we attribute the 0.300 keV line to C V, the 0.470 keV line to N VII, and the 0.580 and 0.686 keV lines to O VII and O VIII, respectively (see Figure 7). There are small excesses in the 0.900–1.1 keV region that we attribute to Ne IX and Ne X. The oxygen lines give us an O^{8+}/O^{7+} ion ratio of 2.0 ± 1.3, which is significantly higher than 0.16 ± 0.07, as measured by ACE/SWICS and the Chandra epoch 1 measurement of 0.05 ± 0.08. Such a high value requires a high solar wind freeze-in temperature; for example, the highest value ratio previously found was $O^{8+}/O^{7+} \sim 1$ for 153P/Ikeya-Zhang, which was attributed to an encounter with an ICME (Bodewits et al. 2007). We attribute our result for comet 46P to the faintness of the comet, poor signal-to-noise, and the poorly resolved O^{7+} feature at 586 eV, possibly because of the loss of low energy sensitivity of ACIS-S. According to ACE and SOHO, 46P encountered a 50% lower proton density ($n_p = 2.9 \pm 0.2$), comparable solar wind speed ($v_{He^{++}} = 401 \pm 6$ km s^{-1}), and a five times higher O^{8+}/O^{7+} ratio compared with epoch 1. At the same time, the $O^{7,8+}/O^{6+}$ ratio was lower during this epoch by about 30%, suggesting that the solar wind contained less O^{7+} but more O^{8+} ions with respect to the previous epoch. This is consistent with the observed X-ray spectrum, which shows a strong O VIII feature and a relatively weak O VII feature (see Figure 7). The X-ray flux observed by Chandra of $F_X = (6.9 \pm 0.5) \times 10^{-13}$erg cm^{2}s^{-1} corresponds to an X-ray luminosity $L_X = (1.23 \pm 0.09) \times 10^{13}$erg s^{-1}, ~4 times lower than the upper limit from the near-simultaneous Swift/XRT observations. The observed X-ray luminosity is a factor of 4.7 lower than during the first epoch, which seems to be mostly driven by the lower solar wind flux and low O^{7+} ion content.

3.3. Epoch 3: 2019 January 12–13

During epoch 3, only Swift observed comet 46P. Similar to epoch 2, no clear X-ray morphology was observed (i.e., no clear transition in the count-rate radial profile as a function of the distance from the comet's nucleus). Considering that a significant part of the coma was within the FoV (approximately 100,000 km), we conclude that the comet's emission was below the detection threshold of the XRT.

The estimated 3σ upper limit from the background-subtracted count rate (approximately 0.005 *cps*, $0.3 < E < 1.0$ keV) translates into a flux upper limit of 1.38×10^{-13} erg cm^{-2} s^{-1} ($L_X < 1.36 \times 10^{13}$ erg s^{-1}), close to the X-ray luminosity measured by Chandra during epoch 2. We note that, in the considered energy range, these values are only weakly dependent on the emission model, and we opted for the simplest one (power law), which also returns the highest probability. Using a power law with spectral index equal to 4 ± 2 (the best fit to the background-subtracted spectrum), the 3σ upper limit would be in the range $1.2 - 1.6 \times 10^{-13}$ erg cm^{-2} s^{-1}.

Compared with epochs 1 and 2, in epoch 3, the comet had a greater distance from Earth ($\Delta \simeq 0.19$ au), and ACE reported a solar wind density and velocity comparable to epoch 2 but lower values for highly ionized oxygen abundances ($O^{7,8+}/O^{6+} = 0.11 \pm 0.03$, $O^{8+}/O^{7+} = 0.06 \pm 0.05$), indicating that the solar wind contained more O^{7+} but less O^{8+} than during epoch 2. The comet's water production was the lowest ($Q_{H_2O} = (0.78 \pm 0.01) \times 10^{28}$ molec. s^{-1}) among the three

epochs: about 33% lower than during epoch 2. These factors explain why X-ray flux and luminosity in the 0.3–1.0 keV are fainter in this epoch than in epochs 1 and 2.

4. Discussion

4.1. What Drives The X-Ray Variability?

It has long been established that the dominant process for X-ray emission by comets is solar wind charge exchange, as corroborated by the spectral characteristics, morphology, and variation of the emission (Cravens 1997; Krasnopolsky 1997). The emissivitiy (and thus the luminosity, because comets are optically thin in X-ray) of charge exchange-induced emission from comets depends on many parameters, including the neutral gas density, the solar wind bulk velocity, density, and fractional ion content, the charge state of these ions, and the emission cross-sections of the relevant charge exchange reactions (e.g., Schwadron & Cravens 2000; Kharchenko & Dalgarno 2001; Bodewits et al. 2007). These properties can be interrelated; as comets approach the Sun, the solar wind density increases with the inverse of the heliocentric distance squared, $1/r_h^2$, while at the same time, the increased solar radiation results in higher gas-production rates, typically at much steeper rates, which peak on or around perihelion (e.g., Combi et al. 2019b). Solar wind velocities, densities, and their ion content are related (Schwadron & Cravens 2000; Bodewits et al. 2007). Charge-exchange emission cross-sections depend on both the solar wind velocity and neutral molecules present in the coma (e.g., Bodewits et al. 2004; Mullen et al. 2017; Cumbee et al. 2018). Finally, below production rates of several times 10^{28} molec. s^{-1}, cometary atmospheres are collisionally thin to charge exchange, except for the inner few thousands of kilometers (Lisse et al. 2005; Bodewits et al. 2007), and not all solar wind ions produce X-rays. In the opposite scenario for an extremely active comet, solar wind ions may go through multiple electron captures and emit several photons (each subsequent photon at a different, lower ionization state), and the X-ray luminosity no longer increases linearly with the comet's neutral gas-production rate (Lisse et al. 1999).

During our campaign, we measured a maximum X-ray luminosity of $5.0 \pm 0.4 \times 10^{13}$ erg s^{-1} during epoch 1 and an upper limit of 1.4×10^{13} erg s^{-1} during epoch 3, corresponding to 5.0–1.4 MW. This makes 46P one of the faintest comets detected in X-rays to date (Wolk et al. 2009; Lisse et al. 2013), with most comets having L_X between 10^{14} and 10^{16} erg s^{-1}. The first reason for 46P's low X-ray luminosity is that the comet had a relatively low gas-production rate, in the order of $0.5–1.2 \times 10^{28}$ molec. s^{-1} (Section 3.3), which is comparable to other comets with low X-ray luminosities observed by Chandra, such as 73P/Schwassmann-Wachmann 3 fragment B (Wolk et al. 2009) and 103P/Hartley 2 (Lisse et al. 2013). This low gas-production rate was combined with unfavorable solar wind conditions during our observations, resulting in the observed relatively low X-ray luminosity.

The properties of both comets and the solar wind can vary at different timescales. Cometary activity varies as different parts of their nucleus face the Sun, resulting in large seasonal variations (weeks to months; Keller et al. 2015) and smaller rotational variations (hours to days, for example; Bodewits et al. 2018). These regular patterns may be disrupted by unexpected, irregular transient behavior, such as outbursts and/or disruptive fragmentation events that can alter cometary activity levels by orders of magnitudes for periods as short as minutes to many weeks (Hughes 1990). The activity levels of Jupiter-family comets tend to vary gradually but can also vary significantly from one apparition to the next. The Sun's atmosphere and the solar wind also vary on multiple timescales (Tindale & Chapman 2017). Solar flares last 10–20 minutes (Veronig et al. 2002). At 1 au, corotating interaction regions on average last 36.7 ± 0.9 h (Jian et al. 2011), whereas the disruption by interplanetary coronal mass ejections can last multiple days (Prise et al. 2015). Finally, the 11 yr solar cycle affects the activity of the Sun, with the solar wind organized bimodally during solar minimum but in a much more chaotic state during solar maximum.

There are not many long-term, high-cadence temporal comet X-ray studies (e.g., Neugebauer et al. 2000; Willingale et al. 2006; Lisse et al. 2007) and even fewer contemporaneous X-ray and gas studies (e.g., Carter et al. 2012). Although Chandra, Swift-UVOT, and Swift-XRT observed the Deep Impact event simultaneously over an extended period, to date, their results have unfortunately not been combined (Willingale et al. 2006; Lisse et al. 2007; Mason et al. 2007).

To interpret the results of our monitoring campaign of 46P, we combined different observations of the relevant properties of the solar wind and comet to empirically estimate the variation of the X-ray flux of the comet (top plot of Figure 8) using the product $n_p \cdot v_{He^{++}} \cdot O^{7,8+}/O^{6+} \cdot Q_{H_2O}$, where $O^{7,8+}/O^{6+}$ is the ratio between O^{7+} and O^{8+} to O^{6+}, and Q_{H_2O} is the water-production rate. This relation for the X-ray luminosity/flux is valid for collisionally thin comae, while in the case of collisionally thick comae, the X-ray flux is independent from the gas-production rate.

To complement our Swift-UVOT observations, we combined different measurements of the comet's water-production rates to cover the entire period of our observations. We used the water-production rates derived from SOHO/Solar Wind ANisotropy (SWAN) observations of the Ly-α emission of atomic hydrogen, as measured by Combi et al. (2019a) during the 2008 (measured at smaller r_h) and 2018 apparitions (measured at larger r_h). These production rates are daily averages that may not represent the possibly significant diurnal variation of the production rates. The nucleus has a rotation period of approximately 9 hr (Farnham et al. 2021), and night-to-night variations in the comet's water-production rate as large as 20% have been measured (Bonev et al. 2021). To fill in the period around perihelion, we used water-production rates based on observations of H_2O from SOFIA (Lis et al. 2019), and of OH from Lowell Observatory (Knight et al. 2021). As was noted by other authors (see Knight et al. 2021), the water production during the 2018 apparition is significantly lower than the rates during its previous apparitions. During the six weeks of our observing campaign, the water-production rates appear to be relatively constant within a factor of 2 (see Figure 8).

We scaled the resulting proxy for the X-ray variation to best match our measured X-ray fluxes and the result is shown in the top panel of Figure 8. The result provides a good, quantitative explanation of the observed X-ray fluxes. At first glance, solar wind conditions were rather similar during the three epochs, with a bulk velocity between 300–400 km s^{-1}. Solar wind proton densities during epoch 1 were twice as high as those observed in epochs 2 and 3; but the charge state of oxygen ions was significantly higher in epoch 2, resulting in a distinct

Table 4
Comparison between Optical Luminosities from Swift/UVOT and X-Ray Luminosities from Swift/XRT and Chandra/ACIS

	Swift/UVOT	Swift/XRT		Chandra/ACIS	
	L_V (10^{16} erg s^{-1})	L_X (10^{13} erg s^{-1})	L_X/L_V (10^{-4})	L_X (10^{13} erg s^{-1})	L_X/L_V (10^{-4})
Epoch 1	6.08 ± 0.18	5.0 ± 0.4	8.3 ± 0.6	5.6 ± 1.8	9 ± 3
Epoch 2	7.9 ± 0.2	<4.8	<6.1	1.23 ± 0.09	1.53 ± 0.12
Epoch 3	4.3 ± 0.2	<1.4			
lt3.2	...	...			

Note. L_V is measured using the V-band filter using an aperture with a radius of 10,000 km. L_X is measured in the 0.3–1.0 keV energy range using the variable apertures described in Section 2.

spectral change with strong O VIII. Epoch 3 saw the same low proton densities as epoch 2, and a charge state closer to epoch 1. Combined with decreasing gas-production rates, this resulted in a very low X-ray luminosity.

During the span of the observations, the X-ray flux has a relative minimum to maximum variation of ~75. The expected peak X-ray flux during the period of our observations likely occurred a week after perihelion, where the peak of the production rate serendipitously coincided with the comet's proximity to Earth and a peak in the solar wind ion flux. It is interesting to note that the temporal trend of the comet's water-production rate is not evident in the predicted X-ray flux, of which the variation is more than one order of magnitude (factor of 75) larger than the Q_{H_2O} fluctuations (factor of 2). Consequently, the overall X-ray variability seems to be driven mostly by solar wind parameters rather than coma properties. The solar wind parameters vary according to the following minimum to maximum intervals: $n_p = 0.84 - 26\,\mathrm{cm}^{-3}$ (factor of 30), $v_{He^{++}} = 270 - 640\,\mathrm{km\,s}^{-1}$ (factor of 2.4), and $O^{7,8+}/O^{6+} = 0.053 - 0.36$ (factor of 7). The proton density and oxygen charge state variations follow each other closely and are the prime driver of mostly short-lived enhancements of the X-ray flux. Regarding the non-detection of the comet by Swift/XRT during the third epoch, had the observations occurred a couple of days earlier (January 5) or later (January 15), the comet might have been an order of magnitude brighter.

4.2. The Relation between Optical and X-ray Luminosities

As optically thin, extended sources, comets generally have high X-ray luminosities relative to their optical luminosities when compared to other objects in our solar system (Dennerl et al. 1997; Ezoe et al. 2011; Lisse et al. 2013). A comparison between optical luminosities, as measured in the Swift/UVOT V-band, and X-ray luminosities is shown in Table 4. Compared with other comets, 46P had both a low X-ray luminosity and low optical luminosity. Its L_x/L_V ratio between 1.5 and 9×10^{-4} (Table 4) is among the highest measured but similar to the ratios measured for several other comets measured by Chandra and ROSAT (Dennerl et al. 1997; Lisse et al. 2013).

We note that the measurements of both the X-ray and optical total luminosities are somewhat uncertain and depend on the method and instruments used. The optical luminosity L_V depends strongly on the bandpass of the filter and the size of the aperture used (gas and dust contribute with different strengths at different wavelengths and aperture sizes). The X-ray flux is strongly dependent on the model used to fit the data, particularly from the low-energy cutoff (where the count rates are generally higher), hence making the comparison between different estimates not always straightforward.

There is no simple relation between the comet's X-ray and optical luminosities. As proposed by Jorda et al. (2008), there is a statistical correlation between the water-production rate and visual magnitude, which is generally satisfied considering a large samples of measurements from different comets. However, there are large differences between individual comets. The dust-to-gas ratio, in particular, shows variation over two orders of magnitude and a strong correlation with the perihelion distance (A'Hearn et al. 1995). Because comet 46P is characterized by a low dust-to-gas ratio (de Almeida et al. 2007) and has a relatively low water-production rate, it has both a relatively low X-ray luminosity and low optical luminosity.

5. Conclusions

X-ray emission from the charge exchange between the solar wind and neutrals in the cometary coma has proven to be a reliable diagnostic for space weather properties, allowing for remote probing of the plasma composition even at locations not accessible by present observatories (e.g., high heliographic latitudes). The monitoring of X-ray and optical/UV emission from comet 46P during the favorable apparition of 2018/2019 allowed for the simultaneous characterization of the X-ray spectrum, from which information on the abundance of solar wind ions can be extracted, and the measurement of water-production rates, which is a proxy of the neutral gaseous particles expanding from the comet's nucleus. The X-ray emission study took advantage of the fact that two different instruments (onboard Swift and Chandra) observed the comet during the same period, making it possible to overcome some technical issues related to the observation strategy and data reduction (mostly inherent to background subtraction) and to compare the results.

Charge exchange-induced emission was detected during the first two epochs (before and at perihelion), while the observations after perihelion do not show a significant excess with respect to the background. The morphology of the X-ray emission before perihelion shows a clump positioned toward the Sun, at approximately 8,000 km from the nucleus' position (after correcting for fore-shortening). The absence of a large-scale crescent shape suggests that the coma is collisionally thin up to distances of about 6,000 km from the nucleus, and the offset of the peak brightness with respect to the nucleus is consistent with the relatively low water-production rate measurements from

Swift/UVOT (1.16 ± 0.01, 1.21 ± 0.04, and $0.78 \pm 0.01 \times 10^{28}$ molec. s^{-1}, respectively).

The spectral analysis of the X-ray emissions during the first two epochs is found to be consistent with the charge-exchange emission models. The measured X-ray flux ($\sim$11, $\sim$7, and $<1 \times 10^{-13}$ erg cm^{-2} s^{-1} for the three epochs, respectively) places 46P among the faintest comets to be detected at these wavelengths. In particular, peaks in the measured spectra are detected at energies consistent with O VII and O VIII emissions, allowing us to infer solar wind properties (i.e., O^{8+}/O^{7+} and solar wind speed) from the X-ray observations. Our estimates are consistent with ACE and SOHO measurements. However, they are affected by large uncertainties as an effect of the low X-ray brightness of the comet: the relative error on the O VIII emission is very high after subtracting the contribution from O VII in the third peak (see component C in 4).

The observed variability in comet properties (i.e., the gas density) is found to be much lower than that in the solar wind itself (i.e., speed, density, and ionization state), confirming the fact that X-ray detection is mostly affected by the local space weather conditions than by the behavior of the comet. These two factors also exhibit variations at very different timescales. A deeper understanding of this nexus would be crucial both for the interpretation of the results (e.g., improving the diagnostic performance) and for planning future cometary X-ray observations.

Support for this work was provided by the National Aeronautics and Space Administration through Chandra Award Number 19100360 issued by the Chandra X-ray Center, which is operated by the Smithsonian Astrophysical Observatory for and on behalf of the National Aeronautics Space Administration under contract NAS8-03060 and by the Neil Gehrels Swift GO program (grant No. 80NSSC18K0504).

Appendix
Observation Log

The complete logs and observing geometry of the Swift (Table A1) and Chandra (Table A2) observations used in this study are given here as observations of moving objects are often hard to locate in coordinate-based astrophysical data archives.

Table A1
Swift/XRT and Swift/UVOT Observation Log

OBS_ID	Epoch	Ext.	Mode	Start Date UTC	Stop Date UTC	Exp. (s)	R.A. (deg)	Decl. (deg)	r_h (au)	Δ (au)	Elong. (deg)	Filter
00094318001	1	1	image	2018 Nov 28 T04:03:32.000	2018 Nov 28 T04:05:55.000	141.6	36.510	−23.305	1.074	0.133	128.192	UVM2
00094318002	1	1	event	2018 Nov 28 T04:06:18.000	2018 Nov 28 T04:10:56.000	273.0	36.509	−23.304	1.074	0.133	128.190	V
00094318003	1	1	event	2018 Nov 28 T04:11:19.000	2018 Nov 28 T04:15:55.000	201.9	36.506	−23.304	1.074	0.133	128.187	U
00094319001	1	1	event	2018 Nov 28 T04:16:18.000	2018 Nov 28 T04:20:55.000	272.7	36.502	−23.303	1.074	0.133	128.184	UVW1
00094319004	1	1	event	2018 Nov 28 T04:21:19.000	2018 Nov 28 T04:25:53.000	189.8	36.498	−23.302	1.074	0.133	128.180	V
00094319005	1	1	event	2018 Nov 28 T04:26:18.000	2018 Nov 28 T04:30:53.000	14.7	36.493	−23.299	1.074	0.133	128.177	U
00094320002	1	1	event	2018 Nov 28 T04:31:19.000	2018 Nov 28 T04:35:48.000	88.5	36.490	−23.296	1.074	0.133	128.175	UVW1
00094381001	1	1	image	2018 Nov 30 T00:42:06.000	2018 Nov 30 T00:43:56.000	107.6	37.727	−21.093	1.070	0.125	129.370	U
00094381002	1	1	event	2018 Nov 30 T00:44:19.000	2018 Nov 30 T00:48:55.000	272.4	37.726	−21.092	1.070	0.125	129.369	UVW1
00094381003	1	1	event	2018 Nov 30 T00:49:19.000	2018 Nov 30 T00:53:55.000	272.1	37.724	−21.091	1.070	0.125	129.366	V
00094382001	1	1	event	2018 Nov 30 T00:54:18.000	2018 Nov 30 T00:58:55.000	178.0	37.720	−21.090	1.070	0.125	129.363	U
00094382004	1	1	event	2018 Nov 30 T00:59:18.000	2018 Nov 30 T01:03:55.000	272.7	37.715	−21.088	1.070	0.125	129.359	UVW1
00094382005	1	1	event	2018 Nov 30 T01:04:18.000	2018 Nov 30 T01:08:51.000	103.3	37.711	−21.085	1.070	0.125	129.356	V
00094383002	1	1	event	2018 Nov 30 T01:09:18.000	2018 Nov 30 T01:13:51.000	13.8	37.707	−21.080	1.070	0.125	129.355	U
00094384001	1	1	image	2018 Nov 30 T02:16:19.000	2018 Nov 30 T02:18:55.000	10.7	37.774	−21.007	1.070	0.124	129.420	U
00094384002	1	1	image	2018 Nov 30 T02:19:21.000	2018 Nov 30 T02:22:41.000	163.5	37.773	−21.006	1.070	0.124	129.419	UVW1
00094384002	1	2	image	2018 Nov 30 T02:22:44.000	2018 Nov 30 T02:23:55.000	70.1	37.773	−21.006	1.070	0.124	129.417	UVW1
00094384003	1	1	image	2018 Nov 30 T02:24:18.000	2018 Nov 30 T02:28:54.000	192.5	37.771	−21.006	1.070	0.124	129.416	V
00094384003	1	2	image	2018 Nov 30 T02:28:55.000	2018 Nov 30 T02:28:55.000	0.8	37.769	−21.005	1.070	0.124	129.414	V
00094385001	1	1	image	2018 Nov 30 T02:29:19.000	2018 Nov 30 T02:32:39.000	85.3	37.767	−21.004	1.070	0.124	129.413	U
00094385001	1	2	image	2018 Nov 30 T02:32:42.000	2018 Nov 30 T02:33:56.000	58.9	37.765	−21.004	1.070	0.124	129.411	U
00094385004	1	1	image	2018 Nov 30 T02:34:21.000	2018 Nov 30 T02:37:41.000	196.6	37.763	−21.003	1.070	0.124	129.409	UVW1
00094385004	1	2	image	2018 Nov 30 T02:37:44.000	2018 Nov 30 T02:38:55.000	70.2	37.761	−21.001	1.070	0.124	129.407	UVW1
00094385005	1	1	image	2018 Nov 30 T02:39:24.000	2018 Nov 30 T02:42:44.000	196.6	37.758	−21.000	1.070	0.124	129.406	V
00094385005	1	2	image	2018 Nov 30 T02:42:47.000	2018 Nov 30 T02:43:55.000	67.9	37.756	−20.998	1.070	0.124	129.405	V
00094386002	1	1	image	2018 Nov 30 T02:44:18.000	2018 Nov 30 T02:47:38.000	196.6	37.755	−20.995	1.070	0.124	129.404	U
00094386002	1	2	image	2018 Nov 30 T02:47:41.000	2018 Nov 30 T02:48:55.000	73.3	37.753	−20.993	1.070	0.124	129.404	U
00094387001	1	1	image	2018 Nov 30 T03:52:31.000	2018 Nov 30 T03:54:55.000	142.2	37.821	−20.920	1.069	0.124	129.469	U
00094387002	1	1	event	2018 Nov 30 T03:55:18.000	2018 Nov 30 T03:59:55.000	271.0	37.820	−20.920	1.069	0.124	129.468	UVW1
00094387003	1	1	event	2018 Nov 30 T04:00:18.000	2018 Nov 30 T04:04:55.000	262.3	37.817	−20.919	1.069	0.124	129.465	V
00094388001	1	1	event	2018 Nov 30 T04:05:18.000	2018 Nov 30 T04:09:53.000	148.7	37.813	−20.918	1.069	0.124	129.461	U
00094388004	1	1	event	2018 Nov 30 T04:10:18.000	2018 Nov 30 T04:14:55.000	87.1	37.809	−20.915	1.069	0.124	129.458	UVW1
00094388005	1	1	event	2018 Nov 30 T04:15:18.000	2018 Nov 30 T04:19:49.000	23.8	37.804	−20.912	1.069	0.124	129.455	V
00094389002	1	1	event	2018 Nov 30 T04:20:18.000	2018 Nov 30 T04:24:49.000	13.8	37.801	−20.908	1.069	0.124	129.453	U
00094390001	1	1	image	2018 Nov 30 T05:28:35.000	2018 Nov 30 T05:30:56.000	78.9	37.868	−20.833	1.069	0.124	129.519	U
00094390002	1	1	image	2018 Nov 30 T05:31:21.000	2018 Nov 30 T05:34:41.000	196.6	37.867	−20.833	1.069	0.124	129.518	UVW1
00094390002	1	2	image	2018 Nov 30 T05:34:44.000	2018 Nov 30 T05:35:55.000	70.2	37.866	−20.832	1.069	0.124	129.517	UVW1
00094390003	1	1	image	2018 Nov 30 T05:36:18.000	2018 Nov 30 T05:39:38.000	196.6	37.865	−20.832	1.069	0.124	129.515	V
00094390003	1	2	image	2018 Nov 30 T05:39:41.000	2018 Nov 30 T05:40:55.000	73.3	37.863	−20.831	1.069	0.124	129.513	V
00094391001	1	1	image	2018 Nov 30 T05:41:18.000	2018 Nov 30 T05:44:38.000	196.6	37.861	−20.831	1.069	0.124	129.512	U
00094391001	1	2	image	2018 Nov 30 T05:44:41.000	2018 Nov 30 T05:45:55.000	73.3	37.859	−20.830	1.069	0.124	129.510	U
00094391004	1	1	image	2018 Nov 30 T05:46:24.000	2018 Nov 30 T05:49:43.000	196.6	37.856	−20.828	1.069	0.124	129.508	UVW1
00094391004	1	2	image	2018 Nov 30 T05:49:46.000	2018 Nov 30 T05:50:55.000	68.1	37.854	−20.827	1.069	0.124	129.507	UVW1
00094391005	1	1	image	2018 Nov 30 T05:51:18.000	2018 Nov 30 T05:54:38.000	196.6	37.852	−20.825	1.069	0.124	129.505	V
00094391005	1	2	image	2018 Nov 30 T05:54:41.000	2018 Nov 30 T05:55:55.000	73.0	37.850	−20.823	1.069	0.124	129.504	V
00094392002	1	1	image	2018 Nov 30 T05:56:19.000	2018 Nov 30 T05:59:38.000	196.6	37.848	−20.821	1.069	0.124	129.504	U
00094392002	1	2	image	2018 Nov 30 T05:59:41.000	2018 Nov 30 T06:00:55.000	72.9	37.847	−20.818	1.069	0.124	129.503	U

Table A1
(Continued)

OBS_ID	Epoch	Ext.	Mode	Start Date UTC	Stop Date UTC	Exp. (s)	R.A. (deg)	Decl. (deg)	r_h (au)	Δ (au)	Elong. (deg)	Filter
00094393001	1	1	image	2018 Nov 30 T07:03:34.000	2018 Nov 30 T07:05:55.000	139.2	37.915	−20.746	1.069	0.124	129.570	U
00094393002	1	1	event	2018 Nov 30 T07:06:19.000	2018 Nov 30 T07:10:55.000	271.8	37.915	−20.745	1.069	0.124	129.568	UVW1
00094393003	1	1	event	2018 Nov 30 T07:11:19.000	2018 Nov 30 T07:15:55.000	272.4	37.912	−20.744	1.069	0.124	129.565	V
00094394001	1	1	event	2018 Nov 30 T07:16:18.000	2018 Nov 30 T07:20:53.000	163.4	37.908	−20.743	1.069	0.123	129.562	U
00094394004	1	1	event	2018 Nov 30 T07:21:18.000	2018 Nov 30 T07:25:52.000	92.1	37.904	−20.741	1.069	0.123	129.559	UVW1
00094394005	1	1	event	2018 Nov 30 T07:26:18.000	2018 Nov 30 T07:30:51.000	23.5	37.899	−20.737	1.069	0.123	129.556	V
00094395002	1	1	event	2018 Nov 30 T07:31:18.000	2018 Nov 30 T07:35:51.000	13.9	37.896	−20.733	1.069	0.123	129.554	U
00094396001	1	1	image	2018 Nov 30 T08:39:24.000	2018 Nov 30 T08:41:56.000	14.3	37.963	−20.657	1.069	0.123	129.620	U
00094396002	1	1	image	2018 Nov 30 T08:42:20.000	2018 Nov 30 T08:45:40.000	196.6	37.962	−20.657	1.069	0.123	129.619	UVW1
00094396002	1	2	image	2018 Nov 30 T08:45:43.000	2018 Nov 30 T08:46:55.000	71.5	37.961	−20.657	1.069	0.123	129.618	UVW1
00094396003	1	1	image	2018 Nov 30 T08:47:18.000	2018 Nov 30 T08:50:38.000	196.6	37.960	−20.656	1.069	0.123	129.617	V
00094396003	1	2	image	2018 Nov 30 T08:50:41.000	2018 Nov 30 T08:51:55.000	73.5	37.958	−20.656	1.069	0.123	129.615	V
00094397001	1	1	image	2018 Nov 30 T08:52:19.000	2018 Nov 30 T08:55:39.000	165.8	37.956	−20.655	1.069	0.123	129.613	U
00094397001	1	2	image	2018 Nov 30 T08:55:42.000	2018 Nov 30 T08:56:56.000	59.8	37.954	−20.654	1.069	0.123	129.612	U
00094397004	1	1	image	2018 Nov 30 T08:57:21.000	2018 Nov 30 T09:00:41.000	196.6	37.951	−20.653	1.069	0.123	129.610	UVW1
00094397004	1	2	image	2018 Nov 30 T09:00:43.000	2018 Nov 30 T09:01:55.000	70.8	37.949	−20.651	1.069	0.123	129.608	UVW1
00094397005	1	1	image	2018 Nov 30 T09:02:19.000	2018 Nov 30 T09:05:39.000	196.6	37.947	−20.649	1.069	0.123	129.607	V
00094397005	1	2	image	2018 Nov 30 T09:05:42.000	2018 Nov 30 T09:06:56.000	72.2	37.945	−20.648	1.069	0.123	129.606	V
00094398002	1	1	image	2018 Nov 30 T09:07:20.000	2018 Nov 30 T09:10:39.000	196.6	37.943	−20.645	1.069	0.123	129.605	U
00094398002	1	2	image	2018 Nov 30 T09:10:42.000	2018 Nov 30 T09:11:55.000	71.9	37.942	−20.642	1.069	0.123	129.605	U
00094399001	1	1	image	2018 Nov 30 T11:51:11.000	2018 Nov 30 T11:52:55.000	102.4	38.059	−20.480	1.069	0.123	129.724	U
00094399002	1	1	event	2018 Nov 30 T11:53:18.000	2018 Nov 30 T11:57:55.000	273.0	38.058	−20.479	1.069	0.123	129.723	UVW1
00094399003	1	1	event	2018 Nov 30 T11:58:18.000	2018 Nov 30 T12:02:55.000	272.9	38.056	−20.478	1.069	0.123	129.720	V
00094400001	1	1	event	2018 Nov 30 T12:03:18.000	2018 Nov 30 T12:07:55.000	173.7	38.052	−20.477	1.069	0.123	129.717	U
00094400004	1	1	event	2018 Nov 30 T12:08:19.000	2018 Nov 30 T12:12:56.000	272.4	38.047	−20.474	1.069	0.123	129.713	UVW1
00094400005	1	1	event	2018 Nov 30 T12:13:18.000	2018 Nov 30 T12:17:50.000	100.7	38.043	−20.471	1.069	0.123	129.710	V
00094401002	1	1	event	2018 Nov 30 T12:18:18.000	2018 Nov 30 T12:22:55.000	13.8	38.039	−20.466	1.069	0.123	129.709	U
00094402001	1	1	image	2018 Nov 30 T15:02:15.000	2018 Nov 30 T15:03:55.000	98.6	38.156	−20.300	1.068	0.122	129.830	U
00094402002	1	1	image	2018 Nov 30 T15:04:18.000	2018 Nov 30 T15:07:38.000	196.6	38.155	−20.299	1.068	0.122	129.829	UVW1
00094402002	1	2	image	2018 Nov 30 T15:07:41.000	2018 Nov 30 T15:08:55.000	73.2	38.155	−20.299	1.068	0.122	129.828	UVW1
00094402003	1	1	image	2018 Nov 30 T15:09:21.000	2018 Nov 30 T15:12:41.000	196.6	38.153	−20.298	1.068	0.122	129.826	V
00094402003	1	2	image	2018 Nov 30 T15:12:44.000	2018 Nov 30 T15:13:55.000	70.4	38.151	−20.298	1.068	0.122	129.825	V
00094403001	1	1	image	2018 Nov 30 T15:14:18.000	2018 Nov 30 T15:17:38.000	196.6	38.149	−20.297	1.068	0.122	129.823	U
00094403001	1	2	image	2018 Nov 30 T15:17:41.000	2018 Nov 30 T15:18:55.000	73.3	38.147	−20.296	1.068	0.122	129.821	U
00094403004	1	1	image	2018 Nov 30 T15:19:19.000	2018 Nov 30 T15:22:39.000	196.6	38.145	−20.295	1.068	0.122	129.820	UVW1
00094403004	1	2	image	2018 Nov 30 T15:22:42.000	2018 Nov 30 T15:23:55.000	72.7	38.143	−20.293	1.068	0.122	129.818	UVW1
00094403005	1	1	image	2018 Nov 30 T15:24:19.000	2018 Nov 30 T15:27:39.000	196.6	38.140	−20.292	1.068	0.122	129.816	V
00094403005	1	2	image	2018 Nov 30 T15:27:42.000	2018 Nov 30 T15:28:56.000	72.4	38.138	−20.290	1.068	0.122	129.815	V
00094404002	1	1	image	2018 Nov 30 T15:29:18.000	2018 Nov 30 T15:32:38.000	196.6	38.137	−20.287	1.068	0.122	129.815	U
00094404002	1	2	image	2018 Nov 30 T15:32:41.000	2018 Nov 30 T15:33:55.000	73.0	38.135	−20.285	1.068	0.122	129.814	U
00094405001	1	1	image	2018 Dec 01 T00:35:36.000	2018 Dec 01 T00:37:55.000	137.5	38.452	−19.747	1.068	0.120	130.159	UVW2
00094405002	1	1	event	2018 Dec 01 T00:38:18.000	2018 Dec 01 T00:42:55.000	272.6	38.452	−19.746	1.068	0.120	130.158	UVW1
00094405003	1	1	event	2018 Dec 01 T00:43:18.000	2018 Dec 01 T00:47:55.000	272.2	38.449	−19.745	1.068	0.120	130.155	V
00094406001	1	1	event	2018 Dec 01 T00:48:18.000	2018 Dec 01 T00:52:55.000	164.3	38.445	−19.743	1.068	0.120	130.152	U
00094406004	1	1	event	2018 Dec 01 T00:53:18.000	2018 Dec 01 T00:57:55.000	263.9	38.441	−19.741	1.068	0.120	130.149	UVW1
00094406005	1	1	event	2018 Dec 01 T00:58:18.000	2018 Dec 01 T01:02:52.000	93.9	38.436	−19.737	1.068	0.120	130.146	V

Table A1
(Continued)

OBS_ID	Epoch	Ext.	Mode	Start Date UTC	Stop Date UTC	Exp. (s)	R.A. (deg)	Decl. (deg)	r_h (au)	Δ (au)	Elong. (deg)	Filter
00094407002	1	1	event	2018 Dec 01 T01:03:18.000	2018 Dec 01 T01:07:52.000	13.5	38.433	−19.732	1.068	0.120	130.144	U
00094408001	1	1	image	2018 Dec 01 T03:47:39.000	2018 Dec 01 T03:49:55.000	133.9	38.553	−19.558	1.067	0.120	130.273	UVW2
00094408002	1	1	image	2018 Dec 01 T03:50:19.000	2018 Dec 01 T03:53:38.000	196.6	38.552	−19.557	1.067	0.120	130.272	UVW1
00094408002	1	2	image	2018 Dec 01 T03:53:41.000	2018 Dec 01 T03:54:55.000	72.9	38.552	−19.556	1.067	0.120	130.271	UVW1
00094408003	1	1	image	2018 Dec 01 T03:55:20.000	2018 Dec 01 T03:58:40.000	196.6	38.550	−19.556	1.067	0.120	130.269	V
00094408003	1	2	image	2018 Dec 01 T03:58:43.000	2018 Dec 01 T03:59:55.000	71.3	38.548	−19.555	1.067	0.120	130.268	V
00094409001	1	1	image	2018 Dec 01 T04:00:19.000	2018 Dec 01 T04:03:38.000	196.6	38.546	−19.554	1.067	0.120	130.266	U
00094409001	1	2	image	2018 Dec 01 T04:03:41.000	2018 Dec 01 T04:04:55.000	72.7	38.544	−19.553	1.067	0.120	130.264	U
00094409004	1	1	image	2018 Dec 01 T04:05:20.000	2018 Dec 01 T04:08:39.000	196.6	38.541	−19.552	1.067	0.120	130.263	UVW1
00094409004	1	2	image	2018 Dec 01 T04:08:42.000	2018 Dec 01 T04:09:56.000	72.1	38.539	−19.550	1.067	0.120	130.261	UVW1
00094409005	1	1	image	2018 Dec 01 T04:10:20.000	2018 Dec 01 T04:13:40.000	196.6	38.537	−19.548	1.067	0.120	130.260	V
00094409005	1	2	image	2018 Dec 01 T04:13:43.000	2018 Dec 01 T04:14:56.000	71.6	38.535	−19.546	1.067	0.120	130.259	V
00094410002	1	1	image	2018 Dec 01 T04:15:19.000	2018 Dec 01 T04:18:39.000	196.6	38.533	−19.543	1.067	0.120	130.259	U
00094410002	1	2	image	2018 Dec 01 T04:18:42.000	2018 Dec 01 T04:19:55.000	72.7	38.532	−19.540	1.067	0.120	130.259	U
00094421001	2	1	image	2018 Dec 13 T09:08:48.000	2018 Dec 13 T09:10:56.000	126.0	53.701	10.571	1.055	0.080	151.741	UVW2
00094421002	2	1	event	2018 Dec 13 T09:11:19.000	2018 Dec 13 T09:27:55.000	417.1	53.698	10.597	1.055	0.080	151.745	V
00094422001	2	1	event	2018 Dec 13 T09:28:18.000	2018 Dec 13 T09:32:54.000	121.9	53.689	10.629	1.055	0.080	151.745	UVW1
00094423001	2	1	image	2018 Dec 13 T10:44:49.000	2018 Dec 13 T10:46:55.000	124.1	53.826	10.809	1.055	0.080	151.900	UVW2
00094423002	2	1	image	2018 Dec 13 T10:47:19.000	2018 Dec 13 T10:50:39.000	196.6	53.826	10.817	1.055	0.080	151.902	V
00094423002	2	2	image	2018 Dec 13 T10:50:42.000	2018 Dec 13 T10:54:02.000	196.6	53.824	10.826	1.055	0.080	151.904	V
00094423002	2	3	image	2018 Dec 13 T10:54:05.000	2018 Dec 13 T10:57:27.000	149.7	53.822	10.836	1.055	0.080	151.904	V
00094423002	2	4	image	2018 Dec 13 T10:57:27.000	2018 Dec 13 T11:00:47.000	145.5	53.819	10.846	1.055	0.080	151.904	V
00094423002	2	5	image	2018 Dec 13 T11:00:51.000	2018 Dec 13 T11:03:55.000	117.3	53.816	10.855	1.055	0.080	151.904	V
00094424001	2	1	image	2018 Dec 13 T11:04:18.000	2018 Dec 13 T11:07:38.000	196.6	53.813	10.866	1.055	0.080	151.904	UVW1
00094424001	2	2	image	2018 Dec 13 T11:07:41.000	2018 Dec 13 T11:08:55.000	73.5	53.812	10.873	1.055	0.080	151.904	UVW1
00094425001	2	1	image	2018 Dec 13 T12:19:47.000	2018 Dec 13 T12:21:55.000	126.4	53.951	11.046	1.055	0.080	152.059	UVW2
00094425002	2	1	event	2018 Dec 13 T12:22:19.000	2018 Dec 13 T12:38:55.000	410.6	53.947	11.072	1.055	0.080	152.063	V
00094426001	2	1	event	2018 Dec 13 T12:39:18.000	2018 Dec 13 T12:43:55.000	62.0	53.938	11.104	1.055	0.080	152.063	UVW1
00094427001	2	1	image	2018 Dec 13 T13:57:04.000	2018 Dec 13 T13:57:56.000	50.9	54.076	11.287	1.055	0.079	152.218	UVW2
00094427002	2	1	image	2018 Dec 13 T13:58:19.000	2018 Dec 13 T14:01:42.000	100.3	54.076	11.293	1.055	0.079	152.220	V
00094427002	2	2	image	2018 Dec 13 T14:01:42.000	2018 Dec 13 T14:05:03.000	10.4	54.075	11.302	1.055	0.079	152.221	V
00094427002	2	3	image	2018 Dec 13 T14:05:04.000	2018 Dec 13 T14:08:27.000	7.0	54.072	11.312	1.055	0.079	152.222	V
00094427002	2	4	image	2018 Dec 13 T14:08:27.000	2018 Dec 13 T14:11:57.000	9.6	54.070	11.322	1.055	0.079	152.222	V
00094427002	2	5	image	2018 Dec 13 T14:11:57.000	2018 Dec 13 T14:14:56.000	9.1	54.067	11.332	1.055	0.079	152.221	V
00094428001	2	1	image	2018 Dec 13 T14:15:18.000	2018 Dec 13 T14:18:38.000	178.1	54.064	11.342	1.055	0.079	152.221	UVW1
00094428001	2	2	image	2018 Dec 13 T14:18:41.000	2018 Dec 13 T14:19:57.000	74.5	54.062	11.349	1.055	0.079	152.221	UVW1
00094429001	2	1	image	2018 Dec 13 T15:31:31.000	2018 Dec 13 T15:33:55.000	142.5	54.202	11.525	1.055	0.079	152.376	UVW2
00094429002	2	1	event	2018 Dec 13 T15:34:19.000	2018 Dec 13 T15:50:51.000	356.7	54.198	11.552	1.055	0.079	152.380	V
00094430001	2	1	event	2018 Dec 13 T15:51:18.000	2018 Dec 13 T15:55:57.000	62.5	54.189	11.584	1.055	0.079	152.379	UVW1
00094431001	3	1	image	2019 Jan 12 T09:55:16.000	2019 Jan 12 T09:57:55.000	156.8	129.103	59.358	1.132	0.184	140.706	UVW1
00094431002	3	1	event	2019 Jan 12 T09:58:19.000	2019 Jan 12 T10:14:55.000	980.2	129.097	59.360	1.132	0.185	140.706	V
00094432001	3	1	event	2019 Jan 12 T10:15:20.000	2019 Jan 12 T10:19:56.000	271.6	129.087	59.356	1.132	0.185	140.712	UVW1
00094433001	3	1	image	2019 Jan 12 T11:31:16.000	2019 Jan 12 T11:33:56.000	157.2	129.188	59.352	1.133	0.185	140.699	UVW1
00094433002	3	1	image	2019 Jan 12 T11:34:19.000	2019 Jan 12 T11:37:39.000	196.6	129.187	59.353	1.133	0.185	140.699	V
00094433002	3	2	image	2019 Jan 12 T11:37:42.000	2019 Jan 12 T11:41:01.000	196.6	129.184	59.353	1.133	0.185	140.699	V

Table A1
(Continued)

OBS_ID	Epoch	Ext.	Mode	Start Date UTC	Stop Date UTC	Exp. (s)	R.A. (deg)	Decl. (deg)	r_h (au)	Δ (au)	Elong. (deg)	Filter
00094433002	3	3	image	2019 Jan 12 T11:41:04.000	2019 Jan 12 T11:44:24.000	196.6	129.182	59.353	1.133	0.185	140.700	V
00094433002	3	4	image	2019 Jan 12 T11:44:27.000	2019 Jan 12 T11:47:47.000	196.7	129.178	59.352	1.133	0.185	140.701	V
00094433002	3	5	image	2019 Jan 12 T11:47:50.000	2019 Jan 12 T11:50:55.000	182.8	129.176	59.351	1.133	0.185	140.703	V
00094434001	3	1	image	2019 Jan 12 T11:51:19.000	2019 Jan 12 T11:54:39.000	196.6	129.173	59.350	1.133	0.185	140.705	UVW1
00094434001	3	2	image	2019 Jan 12 T11:54:42.000	2019 Jan 12 T11:55:56.000	72.8	129.171	59.348	1.133	0.185	140.707	UVW1
00094435001	3	1	image	2019 Jan 12 T13:05:49.000	2019 Jan 12 T13:08:56.000	183.3	129.273	59.344	1.133	0.185	140.693	UVW1
00094435002	3	1	event	2019 Jan 12 T13:09:19.000	2019 Jan 12 T13:25:55.000	979.9	129.267	59.346	1.133	0.185	140.693	V
00094436001	3	1	event	2019 Jan 12 T13:26:18.000	2019 Jan 12 T13:30:55.000	272.8	129.257	59.343	1.133	0.185	140.699	UVW1
00094437001	3	1	image	2019 Jan 12 T14:41:51.000	2019 Jan 12 T14:44:55.000	181.7	129.357	59.337	1.133	0.186	140.686	UVW1
00094437002	3	1	image	2019 Jan 12 T14:45:18.000	2019 Jan 12 T14:48:38.000	196.6	129.356	59.338	1.133	0.186	140.686	V
00094437002	3	2	image	2019 Jan 12 T14:48:41.000	2019 Jan 12 T14:52:01.000	196.6	129.354	59.339	1.133	0.186	140.686	V
00094437002	3	3	image	2019 Jan 12 T14:52:04.000	2019 Jan 12 T14:55:24.000	196.6	129.351	59.339	1.133	0.186	140.686	V
00094437002	3	4	image	2019 Jan 12 T14:55:27.000	2019 Jan 12 T14:58:47.000	196.6	129.348	59.338	1.133	0.186	140.688	V
00094437002	3	5	image	2019 Jan 12 T14:58:50.000	2019 Jan 12 T15:01:56.000	183.0	129.345	59.337	1.133	0.186	140.690	V
00094438001	3	1	image	2019 Jan 12 T15:02:18.000	2019 Jan 12 T15:05:38.000	196.6	129.342	59.336	1.133	0.186	140.692	UVW1
00094438001	3	2	image	2019 Jan 12 T15:05:42.000	2019 Jan 12 T15:06:55.000	71.9	129.340	59.334	1.133	0.186	140.694	UVW1
00094439001	3	1	image	2019 Jan 12 T16:17:49.000	2019 Jan 12 T16:20:55.000	183.2	129.441	59.330	1.134	0.186	140.680	UVW1
00094439002	3	1	event	2019 Jan 12 T16:21:18.000	2019 Jan 12 T16:37:55.000	981.4	129.434	59.331	1.134	0.186	140.680	V
00094440001	3	1	event	2019 Jan 12 T16:38:18.000	2019 Jan 12 T16:42:55.000	272.6	129.425	59.328	1.134	0.186	140.686	UVW1
00094441001	3	1	image	2019 Jan 12 T17:52:50.000	2019 Jan 12 T17:55:55.000	182.6	129.525	59.323	1.134	0.186	140.674	UVW1
00094441002	3	1	image	2019 Jan 12 T17:56:20.000	2019 Jan 12 T17:59:40.000	196.6	129.523	59.324	1.134	0.186	140.673	V
00094441002	3	2	image	2019 Jan 12 T17:59:44.000	2019 Jan 12 T18:03:03.000	196.6	129.521	59.324	1.134	0.186	140.673	V
00094441002	3	3	image	2019 Jan 12 T18:03:06.000	2019 Jan 12 T18:06:26.000	196.6	129.518	59.324	1.134	0.186	140.674	V
00094441002	3	4	image	2019 Jan 12 T18:06:29.000	2019 Jan 12 T18:09:49.000	196.6	129.515	59.324	1.134	0.186	140.675	V
00094441002	3	5	image	2019 Jan 12 T18:09:52.000	2019 Jan 12 T18:12:55.000	180.6	129.512	59.323	1.134	0.186	140.677	V
00094442001	3	1	image	2019 Jan 12 T18:13:18.000	2019 Jan 12 T18:16:38.000	196.6	129.509	59.321	1.134	0.187	140.679	UVW1
00094442001	3	2	image	2019 Jan 12 T18:16:41.000	2019 Jan 12 T18:17:55.000	73.2	129.508	59.320	1.134	0.187	140.681	UVW1
00094443001	3	1	image	2019 Jan 12 T21:06:58.000	2019 Jan 12 T21:09:56.000	174.7	129.689	59.308	1.135	0.187	140.662	UVW1
00094443002	3	1	event	2019 Jan 12 T21:20:02.000	2019 Jan 12 T21:26:55.000	407.0	129.677	59.307	1.135	0.187	140.666	V
00094444001	3	1	event	2019 Jan 12 T21:27:19.000	2019 Jan 12 T21:31:57.000	270.7	129.672	59.304	1.135	0.187	140.670	UVW1
00094459001	3	1	image	2019 Jan 13 T00:25:15.000	2019 Jan 13 T00:26:56.000	98.9	129.848	59.294	1.135	0.188	140.651	U
00094459002	3	1	image	2019 Jan 13 T00:27:19.000	2019 Jan 13 T00:30:39.000	196.6	129.845	59.293	1.135	0.188	140.652	V
00094459002	3	2	image	2019 Jan 13 T00:30:42.000	2019 Jan 13 T00:34:01.000	196.6	129.842	59.293	1.135	0.188	140.653	V
00094459002	3	3	image	2019 Jan 13 T00:34:04.000	2019 Jan 13 T00:37:24.000	196.6	129.839	59.291	1.135	0.188	140.655	V
00094459002	3	4	image	2019 Jan 13 T00:37:27.000	2019 Jan 13 T00:40:47.000	196.6	129.837	59.290	1.135	0.188	140.658	V
00094459002	3	5	image	2019 Jan 13 T00:40:50.000	2019 Jan 13 T00:43:55.000	182.7	129.835	59.288	1.135	0.188	140.660	V
00094460001	3	1	image	2019 Jan 13 T00:44:18.000	2019 Jan 13 T00:47:38.000	196.6	129.834	59.286	1.135	0.188	140.663	UVW1
00094460001	3	2	image	2019 Jan 13 T00:47:41.000	2019 Jan 13 T00:48:55.000	73.0	129.834	59.284	1.135	0.188	140.665	UVW1
00094461001	3	1	image	2019 Jan 13 T03:27:07.000	2019 Jan 13 T03:29:56.000	166.0	130.015	59.276	1.136	0.189	140.640	U
00094461002	3	1	event	2019 Jan 13 T03:30:18.000	2019 Jan 13 T03:46:55.000	981.4	130.009	59.278	1.136	0.189	140.641	V
00094462001	3	1	event	2019 Jan 13 T03:47:18.000	2019 Jan 13 T03:51:55.000	272.8	129.999	59.274	1.136	0.189	140.646	UVW1
00094463001	3	1	image	2019 Jan 13 T06:38:07.000	2019 Jan 13 T06:40:55.000	165.8	130.175	59.260	1.136	0.190	140.630	U
00094463002	3	1	image	2019 Jan 13 T06:41:18.000	2019 Jan 13 T06:44:38.000	196.6	130.174	59.261	1.137	0.190	140.630	V
00094463002	3	2	image	2019 Jan 13 T06:44:41.000	2019 Jan 13 T06:48:01.000	196.6	130.172	59.261	1.137	0.190	140.630	V
00094463002	3	3	image	2019 Jan 13 T06:48:06.000	2019 Jan 13 T06:51:25.000	196.6	130.169	59.261	1.137	0.190	140.631	V
00094463002	3	4	image	2019 Jan 13 T06:51:28.000	2019 Jan 13 T06:54:48.000	196.6	130.166	59.261	1.137	0.190	140.632	V

Table A1
(Continued)

OBS_ID	Epoch	Ext.	Mode	Start Date UTC	Stop Date UTC	Exp. (s)	R.A. (deg)	Decl. (deg)	r_h (au)	Δ (au)	Elong. (deg)	Filter
00094463002	3	5	image	2019 Jan 13 T06:54:51.000	2019 Jan 13 T06:57:55.000	181.4	130.163	59.260	1.137	0.190	140.633	V
00094464001	3	1	image	2019 Jan 13 T06:58:18.000	2019 Jan 13 T07:01:38.000	196.6	130.160	59.258	1.137	0.190	140.636	UVW1
00094464001	3	2	image	2019 Jan 13 T07:01:41.000	2019 Jan 13 T07:02:55.000	73.2	130.158	59.257	1.137	0.190	140.637	UVW1

Note. ext.: every observation consists of one or more exposures, which are recorded by different extensions in the observation's fits file, ext. means the exposure's extension ID; **exp.**: exposure time; **RA** and **Dec**: R.A. and decl. of the comet at the midtime of the exposure; r_h: heliocentric distance; Δ: geocentric distance; **elong.**: elongation angle; **filter**: the filter used by UVOT for the exposure. UVOT data acquired using UVM2, UVW2, and U filters were not used in this analysis. XRT observed the comet in sync with all UVOT exposures and the entire XRT data set was used in data analyses.

(This table is available in machine-readable form.)

Table A2
Chandra/ACIS Observation Log

OBS_ID	Epoch	Start Date UTC	Exposure (s)	RA (deg)	Dec (deg)	r_h (au)	Δ (au)	Elongation (deg)	Target
20275	1	2018 Dec 03 T18:12:10	9940	40.96[a]	−15.452[a]	…	…	…	background
21977	1	2018 Dec 03 T21:16:05	5110	40.61	−15.584	1.063	0.109	132.6	comet
21978	1	2018 Dec 03 T22:47:54	5120	40.644	−15.454	1.062	0.108	132.7	comet
21979	1	2018 Dec 04 T00:19:45	5110	40.678	−15.32	1.062	0.108	132.8	comet
21980	1	2018 Dec 04 T01:51:35	5120	40.711	−15.18	1.062	0.108	132.9	comet
21981	1	2018 Dec 04 T03:23:25	11220	41.062[a]	−15.038[a]	…	…	…	background
21982	2	2018 Dec 13 T05:56:31	9940	54.127[a]	10.197[a]	…	…	…	background
21983	2	2018 Dec 13 T09:06:52	2150	53.614	9.938	1.055	0.08	151.4	comet
21984	2	2018 Dec 13 T09:48:42	2160	53.668	10.03	1.055	0.08	151.4	comet
21985	2	2018 Dec 13 T10:33:43	2150	53.726	10.13	1.055	0.08	151.5	comet
21986	2	2018 Dec 13 T11:21:57	2160	53.788	10.237	1.055	0.08	151.6	comet
21987	2	2018 Dec 13 T12:09:36	2150	53.848	10.344	1.055	0.08	151.6	comet
21988	2	2018 Dec 13 T12:56:32	2160	53.907	10.451	1.055	0.08	151.7	comet
21989	2	2018 Dec 13 T13:43:36	2150	53.966	10.558	1.055	0.08	151.8	comet
21990	2	2018 Dec 13 T14:28:48	2170	54.022	10.662	1.055	0.08	151.8	comet
21991	2	2018 Dec 13 T15:11:18	2150	54.075	10.76	1.055	0.08	151.9	comet
21992	2	2018 Dec 13 T15:56:04	2160	54.13	10.864	1.055	0.08	152	comet
21993	2	2018 Dec 13 T16:40:49	9060	54.65[a]	11.137[a]	…	…	…	background

Note.
[a] Pointing position for background observation.

ORCID iDs

Emanuele Bonamente https://orcid.org/0000-0003-3847-0510
Damian J. Christian https://orcid.org/0000-0003-1746-3020
Zexi Xing (邢泽曦) https://orcid.org/0000-0003-2399-5613
Kumar Venkataramani https://orcid.org/0000-0003-3321-1472
Dimitra Koutroumpa https://orcid.org/0000-0002-5716-3412
Dennis Bodewits https://orcid.org/0000-0002-2668-7248

References

A'Hearn, M. F., Belton, M. J. S., Delamere, A. A., et al. 2011, Sci, 332, 1396
A'Hearn, M. F., Millis, R. C., Schleicher, D. O., Osip, D. J., & Birch, P. V. 1995, Icar, 118, 223
Allen, R. C., Lario, D., Odstrcil, D., et al. 2020, ApJS, 246, 36
Arnaud, K. A. 1996, adass, 101, 17
Bodewits, D., Christian, D., Kelley, M., et al. 2019, EPSC-DPS Joint Meeting 2019, EPSC-DPS2019-761
Bodewits, D., Christian, D. J., Torney, M., et al. 2007, A&A, 469, 1183
Bodewits, D., Farnham, T. L., A'Hearn, M. F., et al. 2014, ApJ, 786, 48
Bodewits, D., Farnham, T. L., Kelley, M. S., & Knight, M. M. 2018, Natur, 553, 186
Bodewits, D., Juhasz, Z., Hoekstra, R., & Tielens, A. G. G. M. 2004, ApJ, 606, L81
Bonev, B. P., Dello Russo, N., DiSanti, M. A., et al. 2021, PSJ, 2, 45
Breeveld, A. A., Curran, P. A., Hoversten, E. A., et al. 2010, MNRAS, 406, 1687
Breeveld, A. A., Landsman, W., Holland, S. T., et al. 2011, in AIP Conf. Ser., 1358, Gamma Ray Bursts, ed. J. E. McEnery, J. L. Racusin, & N. Gehrels (Melville, NY: AIP), 373
Burrows, D. N., Hill, J. E., Nousek, J. A., et al. 2005, SSRv, 120, 165
Busemann, H., Nguyen, A. N., Cody, G. D., et al. 2009, E&PSL, 288, 44
Carter, J. A., Bodewits, D., Read, A. M., & Immler, S. 2012, A&A, 541, A70
Cash, W. 1979, ApJ, 228, 939
Christian, D. J., Bodewits, D., Lisse, C. M., et al. 2010, ApJS, 187, 447
Combi, M. R., Mäkinen, T. T., Bertaux, J.-L., Quémerais, E., & Ferron, S. 2019a, Icar, 317, 610
Combi, M. R., Shou, Y., Feaga, L. M., & Tenishev, V. 2019b, AGUFM, P43C
Cravens, T. E. 1997, GeoRL, 24, 105
Cravens, T. E. 2002, Sci, 296, 1042
Cumbee, R. S., Mullen, P. D., Lyons, D., et al. 2018, ApJ, 852, 7
de Almeida, A. A., Sanzovo, G. C., Singh, P. D., et al. 2007, AdSpR, 39, 432
Dennerl, K., Englhauser, J., & Trümper, J. 1997, Sci, 277, 1625
DiSanti, M. A., Dello Russo, N., Bonev, B. P., et al. 2017, AAS/DPS, 49, 305.03
Ezoe, Y., Ishikawa, K., Ohashi, T., et al. 2011, AdSpR, 47, 411
Farnham, T. L., Knight, M. M., Schleicher, D. G., et al. 2021, PSJ, 2, 7
Farnham, T. L., & Schleicher, D. G. 1998, A&A, 335, L50
Fruscione, A., McDowell, J. C., Allen, G. E., et al. 2006, Proc. SPIE, 6270, 62701V
Fulle, M. 2000, Icar, 145, 239
Garmire, G. P., Bautz, M. W., Ford, P. G., Nousek, J. A., & Ricker, G. R., Jr. 2003, Proc. SPIE, 4851, 28
Gehrels, N. 2004, in ESA SP-552, Proc. of the 5th INTEGRAL Workshop on the INTEGRAL Universe, ed. V. Schönfelder, G. Lichti, & C. Winkler (Paris: ESA), 777
Glassmeier, K.-H., Boehnhardt, H., Koschny, D., Kührt, E., & Richter, I. 2007, SSRv, 128, 1
Gloeckler, G., Cain, J., Ipavich, F. M., et al. 1998, SSRv, 86, 497
Hovestadt, D., Bochsler, P., Grünwaldt, H., et al. 1995, LNP, 444, 271
Hughes, D. W. 1990, QJRAS, 31, 69
Jian, L. K., Russell, C. T., Luhmann, J. G., et al. 2011, SoPh, 273, 179
Jorda, L., Crovisier, J., & Green, D. W. E. 2008, LPICo, 1405, 8046
Kaaret, P., Koutroumpa, D., Kuntz, K. D., et al. 2020, NatAs, 4, 1072
Keller, H. U., Mottola, S., Davidsson, B. J. R., et al. 2015, A&A, 583, A34
Kharchenko, V., & Dalgarno, A. 2001, ApJ, 554, L99
Knight, M. M., Schleicher, D. G., & Farnham, T. L. 2021, PSJ, 2, 104
Koutroumpa, D. 2012, AN, 333, 341
Koutroumpa, D., Lallement, R., Kharchenko, V., et al. 2006, A&A, 460, 289
Krasnopolsky, V. A. 1997, Icar, 128, 368
Krasnopolsky, V. A., Mumma, M. J., & Abbott, M. J. 2000, Icar, 146, 152
Lamy, P. L., Toth, I., Jorda, L., Weaver, H. A., & A'Hearn, M. 1998, A&A, 335, L25
Lepri, S. T., Landi, E., & Zurbuchen, T. H. 2013, ApJ, 768, 94
Lis, D. C., Bockelée-Morvan, D., Güsten, R., et al. 2019, A&AS, 625, L5
Lisse, C. M., Christian, D. J., Dennerl, K., et al. 1999, Icar, 141, 316
Lisse, C. M., Christian, D. J., Dennerl, K., et al. 2001, Sci, 292, 1343
Lisse, C. M., Christian, D. J., Dennerl, K., et al. 2005, ApJ, 635, 1329
Lisse, C. M., Christian, D. J., Wolk, S. J., et al. 2013, Icar, 222, 752
Lisse, C. M., Dennerl, K., Christian, D. J., et al. 2007, Icar, 190, 391
Lisse, C. M., Dennerl, K., Englhauser, J., et al. 1996, Sci, 274, 205
Masci, F. 2011, Computing Flux Upper-limits for Non-detections, http://wise2.ipac.caltech.edu/staff/fmasci/UpperLimits_FM2011.pdf
Mason, K. O., Chester, M. M., Cucchiara, A., et al. 2007, Icar, 187, 123
McComas, D. J., Bame, S. J., Barker, P., et al. 1998, SSRv, 86, 563
Meech, K. J., Bauer, J. M., & Hainaut, O. R. 1997, A&A, 326, 1268
Miller, C. J., Nichol, R. C., Wasserman, L., et al. 2001, BAAS, 33, 826

Mullen, P. D., Cumbee, R. S., Lyons, D., et al. 2017, ApJ, 844, 7
Neugebauer, M., Cravens, T. E., Lisse, C. M., et al. 2000, JGR, 105, 20949
Nevalainen, J., David, L., & Guainazzi, M. 2010, A&A, 523, A22
Noonan, J. W., Harris, W. M., Bromley, S., et al. 2021, PSJ, 2, 8
Plucinsky, P. P., Bogdan, A., Germain, G., & Marshall, H. L. 2016, Proc. SPIE, 9905, 990544
Pollack, J. B., & Yung, Y. L. 1980, AREPS, 8, 425
Poole, T. S., Breeveld, A. A., Page, M. J., et al. 2008, MNRAS, 383, 627
Prise, A. J., Harra, L. K., Matthews, S. A., Arridge, C. S., & Achilleos, N. 2015, JGRA, 120, 1566
Richardson, I. G., & Cane, H. V. 2010, SoPh, 264, 189
Romano, P., Cusumano, G., Campana, S., et al. 2005, Proc. SPIE, 5898, 369
Roming, P. W., Kennedy, T. E., Mason, K. O., et al. 2005, SSRv, 120, 95
Rubin, M., Bekaert, D. V., Broadley, M. W., Drozdovskaya, M. N., & Wampfler, S. F. 2019, ACS Earth and Space Chemistry, 3, 1792
Schleicher, D. G., & A'Hearn, M. F. 1988, ApJ, 331, 1058
Schwadron, N. A., & Cravens, T. E. 2000, ApJ, 544, 558
Schwehm, G., & Schulz, R. 1999, SSRv, 90, 313
Snios, B., Kharchenko, V., Lisse, C. M., et al. 2016, ApJ, 818, 199
Stern, S. A., Parker, J. W., Festou, M. C., et al. 1998, A&AS, 335, L30
Tindale, E., & Chapman, S. C. 2017, JGRA, 122, 9824
Veronig, A., Temmer, M., Hanslmeier, A., Otruba, W., & Messerotti, M. 2002, A&A, 382, 1070
Warner, E., A'Hearn, M. F., Bodewits, D., et al. 2016, AAS/DPS Meeting, 48, 217.14
Weisskopf, M. C., Tananbaum, H. D., Van Speybroeck, L. P., & O'Dell, S. L. 2000, Proc. SPIE, 4012, 2
Willingale, R., O'Brien, P. T., Cowley, S. W. H., et al. 2006, ApJ, 649, 541
Wolk, S. J., Lisse, C. M., Bodewits, D., Christian, D. J., & Dennerl, K. 2009, ApJ, 694, 1293